Models, Optimal Performances and Sensitivities of Commercial Flight Trajectory in the Air Traffic System

A THESIS
SUBMITTED TO THE FACULTY OF THE GRADUATE SCHOOL
OF THE UNIVERSITY OF MINNESOTA
BY

Di Wu

IN PARTIAL FULFILLMENT OF THE REQUIREMENTS
FOR THE DEGREE OF
Doctor of Philosophy

Advisor: Yiyuan Zhao

December, 2012

Acknowledgements

There are many people that have earned my gratitude for their contribution to my study and research time in department of Aerospace Engineering and Mechanics.

Let me begin by thanking my Ph.D. advisor, Professor Yiyuan Zhao, for his high-level thinking about trajectory optimization with its application in Air Traffic Control system, for obtaining support, for his comments, and enthusiasm throughout the course of the research, and for helping me organize this thesis. Prof. Zhao's positive attitude towards personal and professional relationships has been an inspiration to me.

Professors William Garrard, Demoz Gebre-Egziabher, Rajesh Rajamani, and Tryphon Georgiou contributed constructive comments and questions during the final phases of this thesis. Generally, I would like to thank all of the above professors, and many more, for the quality instruction I have received at the University of Minnesota.

I would like to thank Brian Capozzi, and Stephen Pledgie of Mosaic ATM for many discussions on Flight Management Systems, and the philosophy behind their systems.

Qian Zheng, Heming Chen, and others in Air Traffic Control Group shared their thoughts on the analysis of trajectory generation for Air Traffic Flight Management system, and provided me with documentation on surface traffic management system and dynamic models.

I would like to thank my mother, for influencing my values, for giving me the opportunities to pursue the things I value, and for her caring and support during my education.

This research was supported in part by NASA Cooperative Agreement to the University of Minnesota titled Systematically Achieving Accurate, Reliable, and Consistent Trajectory Predictions.

Abstract

This thesis provided systematic modeling foundation for trajectory generation of commercial aircraft flight, examined different choices of performance indices in trajectory generation within Air Traffic Control (ATC) system, and discussed sensitivity concepts to evaluate the qualities of generated optimal trajectories.

The trajectory generation is typically performed by individual aircraft or their airline operation centers to optimize flight performances including flight time or flight distance. Additionally, while aircraft environmental impacts becoming a growing issue for commercial aviation, green aviation is becoming one of the most pressing issues hampering commercial aviation growth today, which also needs to be considered while generating aircraft flight trajectories.

This thesis first systematically analyzes mathematical models of trajectory generation process in ATC system. Complete point-mass equations of motion within consideration of rotating spherical earth are derived. Models of motion intents and guidance strategies of flight trajectory generation are studied next, followed by the modeling of trajectory segments and their tracking objectives. This thesis lays a foundation to modeling framework for airborne flight trajectory process to support trajectory-based operations.

In this thesis, trajectory generation process is formulated as a parameter optimal control problem in consistence with ATC procedures. A gradient algorithm is devised for obtaining numerical solutions. Climb and descent phases are first studied separately, and are then combined, together with cruise phase, to examine complete trajectories from liftoff to touchdown. For climb, decent, and the entire flight, optimal trajectories are calculated that respectively minimize flight time, fuel consumption, emissions, and when applicable, distance traveled, and these optimal trajectories are compared for their trade-offs.

Next, to evaluate qualities of generated optimal trajectories, two sensitivity concepts are used. Open-loop sensitivities measure changes of generated trajectories due to modeling errors, and reflect reliability of the trajectory generation process. In contrast,

closed-loop sensitivities measure deviations of actual trajectories from generated trajectories caused by modeling errors and/or flight conditions, where actual trajectories are obtained with the pilots or autopilots actively tracking flight objectives extracted from the generated trajectories. They reflect trajectory predictability. In this thesis, closed-loop sensitivities are computed with respect to potential uncertainties of vertical wind speed.

Contents

List of Tables

List of Figures

Chapter 1

Introduction

The rapidly increasing air travel has severely burdened the current air traffic control (ATC) infrastructure and created a heavy workload for air traffic controllers. During the same time, growing fuel prices, airline competition, rising public and environmental concerns have heightened the need to save fuel, reduce emissions and noise. It has become increasingly important to develop ATC automation systems to assist controllers in guaranteeing safety, increasing airport throughput, reducing aircraft delays and cutting fleet-wide fuel consumption.

Trajectory generation is the core part of an air traffic control automation system. The trajectory synthesis first computes nominal flight trajectories, including a nominal flight and a minimum and maximum speed flight, for all aircraft within a region. Based the flight region and estimated flight time, the trajectory generation optimizes the trajectories, iterating the flight speed and path as necessary to meet the scheduled time of arrival (TOA) and achieved better flight performances. The trajectories of all aircraft need to be checked to ensure the minimum separations between aircrafts, and changes are made to the trajectories if necessary to resolve conflicts.

The computation of trajectory generation requires aircraft dynamics models, performance models, ambient environmental models, optimization algorithms, and trajectory tracking techniques. This thesis presents the systemic foundation for these modeling components to support trajectory-based operations. Different flight performances including flight time, fuel consumption, emissions, and when applicable, flight distance,

are optimized singely or combined to reveal the optimal performance of trajectory generation, and the trade-offs between them. The quality of generated trajectory is evaluated using the concept of sensitivity analysis.

1.1 Commercial Aircraft Flight Procedure in Air Traffic System

In today's ATC procedures, a complete commercial flight trajectory typically consists of three phases: climb, cruise, and descent, shown in Fig. 1.1. Each phase is in turn composed of a series of flight segments, where each segment is characterized by a set of flight objectives. In other words, a series of selected flight segments constitute a complete trajectory profile. Studies of trajectory planning and prediction in ATC should consider the trajectory structures imposed by these segments and profiles. Therefore, the mathematical representations of these flight segments and profiles are needed.

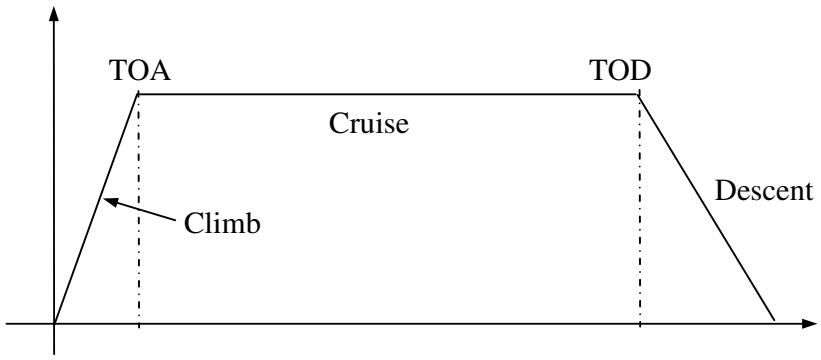

Figure 1.1: Profile of complete flight trajectory.

For a high-speed subsonic commercial transport, representative segments during the climb phase include constant Mach/CAS climb with a constant throttle setting, climb with specified acceleration and throttle setting, and level flight with specified acceleration or throttle setting. Descent flight segments are similar to those of the climb phase in structure. In comparison, the cruise phase can be characterized by segments of level flight with a specified Mach or true airspeed, or cruise climb with constant speed and constant lift coefficient at its optimal value. Summarizing these different cases, a

generic vertical flight segment can be described by specifying two objectives out of the five variable groups, shown in Table. 1.1.

Table 1.1: Mathematical description of flight segments.

Variable Group	Choices	Control	Orders
Speed	M, V_{CAS}, or V_t	T or C_L	1^{st} using T, 2^{nd} using C_L
Accel/Decel	$\dot{V}_t$	T	0^{th}
Throttle	κ	T	0^{th}
Altitude	(h_p, $\dot{h}$, or γ)	C_L	1^{st} for $\dot{h}/\gamma$, 2^{nd} for $\dot{h}_p$
Lift Coefficient	C_L	C_L	0^{th}

A trajectory profile contains a pre-defined sequence of flight segments connected with proper capture conditions. In connecting two segments, a certain monotonic variable during the first segment is declared a capture variable. When this variable reaches a threshold value, the second segment begins. The definition of a trajectory profile not only needs to specify the segments in it, but also the capture conditions used to connect these segments.

In actual flights, the pilot monitors the capture variable while maintaining the objectives of the current segment. When this variable teaches a pre-selected threshold, the pilot switches to follow the flight commands of the next segment. Numerical simulations can imitate this pilot behavior by periodically checking the capture condition. After it is met, current trajectory segment ends and the next segment begins.

1.2 Concept of Trajectory Generation for Commercial Aircraft

The trajectory generation consists of two parts: trajectory planning and trajectory prediction. Trajectory planning is typically performed by individual aircraft or their airline operation centers to optimize flight performances (flight time, fuel consumption, emissions, etc), Fig. 1.2. Trajectory prediction seeks to determine the most likely and reliable future aircraft trajectories for use in Decision Support Tools (DSTs). Accurate trajectory generation is central to trajectory-based operations (TBO) advocated by the Next Generation Air Transportation System [1]. While trajectory planning and prediction may have different access to aircraft state information, ambient conditions, and

pilot intents, they share the same fundamental physics of flight. As a result, algorithms of trajectory planning are often used for trajectory predictions. With the advances in digital datalink, the distinction between the two will become even smaller. In this paper, they are studied together and jointly called trajectory generation.

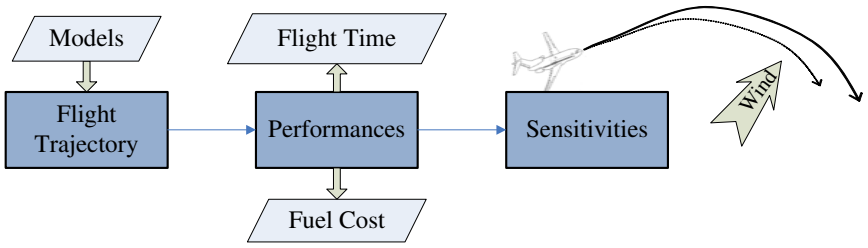

Figure 1.2: Things to do for trajectory generation.

In a trajectory generation process, models of aircraft motion, aircraft performance capabilities, ambient conditions, and flight procedures are needed. These models will necessarily contain errors. Then, based on these models, trajectory solution algorithms are required to obtain solutions, and practical trajectory algorithms can be of varying complexities. In general, more accurate trajectory solutions require higher-fidelity models and/or more sophisticated algorithms, at the expense of increased modeling and computational efforts. However, overly demanding modeling accuracy and/or complicated algorithms may suffer from poorer reliability in addition to larger development costs and longer convergence time, without offering substantial improvements. The key is to provide the right level of modeling fidelity and algorithm sophistication for the right applications [2]. Table. 1.2 presents the typical evaluating criteria for modeling choices.

Table 1.2: Trajectory Model Evaluation Criteria.

Criterion	Descriptions
Accuracy	Small errors from actual trajectory
Computational Speed	Time required to complete computations
Feasibility	Ability to satisfy motion constraints
Complexity	Efforts to develop and to implement
Uncertainty	Modeling Ability to represent uncertainties

In general, trajectory generation in ATC is a dynamic optimization problem. This

thesis formulates the trajectory generation as a parameter optimal control problem. When optimizing, different choices of optimization criteria and their tradeoffs are evaluated for generated trajectories. In obtaining trajectory solutions for different choices of optimization criteria, an iterative numerical scheme is devised that uses up to first-order gradient information. This scheme can also be used to assess the accuracies of any other simplified solution algorithms.

The required sophistication of trajectory algorithms not only depends on the fidelity level of available models, but also on the choice of trajectory optimization criteria. We first examine different meaningful choices of optimization criteria for trajectory generations, and to study the differences in the corresponding generated trajectories. These differences reveal the range of performance benefits possible with optimal trajectory generation. In addition, the amount of improvement during the iterative trajectory generation process demonstrates the levels of optimality that can be achieved with more sophisticated algorithms.

1.3 Trajectory Generation for Environmentally Responsible Aviation

Trajectory generation, as the key part for the automated air traffic control system, is conducted to achieved better flight performance with lower operation cost, including lower flight time and flight fuel consumption. Moreover, the environmental issue of aviation, aircraft emissions and noise have also been of concern since the beginning of commercial aviation. The continuing growth in air traffic and increasing public awareness have made environmental considerations one of the most critical aspects of commercial aviation today. It is generally accepted that significant improvements to the environmental acceptability of aircraft will be needed if the long-term growth of air transport is to be sustained.

Currently, the world fleet releases approximately 13% of CO_2 emissions from all transportation sources, or 2% of all anthropogenic sources [3]. Aircraft emissions currently account for 2-3% of total global emissions and are projected to increase by a factor of 1.6 to 10, depending on the fuel use scenario. Environmentally Responsible

Aviation (ERA), which is a NASA Aeronautics project, seeks to develop ways to mitigate the adverse impacts of aviation on the environment [4]. The motivation of ERA is to increase fuel efficiency, reduce noise and emission impacts. The main mission is to perform research to explore/assess the feasibility, benefits, interdependencies, and risks of vehicle concepts and enabling technologies identified as having potential to mitigate the impact of aviation on the environment . There are 3 main environmental problems of aviation: fuel burn, emissions, and noise. Regulations for aviation-related air quality are assessed by International Civil Aviation Organization (ICAO).

1.3.1 Aircraft Emissions

Importance of reducing emissions released by aircraft around the airport

Around the airport, the release of exhaust gasses in the atmosphere is one of major environmental issues associated with commercial airliners. Current emissions regulations have focused on local air quality in the vicinity of airports. 40 of the top 50 U.S. airports are in non-attainment areas that do not meet local air quality standards for particulate matter and ozone. Main pollutants affecting air quality surrounding airport are NO_x, CO and unburned hydrocarbons. Approximately 56% of all commercial aircraft emissions at lower altitude are in the form of NO_x.

At lower altitude, ICAO have regulations for the landing-takeoff (LTO) cycle up to 915 meters (3,000 feet) above airport runway over NO_x, CO, unburned hydrocarbons, and smoke emissions [5, 6]. During the LTO cycle, approximately 56% of all commercial aircraft emissions are in the form of NO_x. Unburned hydrocarbons typically contribute less than 5%. In fact, significant progress in combustor designs and reducing specific fuel consumption have almost eliminated the issue of particulate matter emissions. Therefore, NO_x reduction during LTO cycle is currently the major environmental problem around the airport.

Current regulations on emissions focus on local air quality in the vicinity of airports. For example, the International Civil Aviation Organization (ICAO) has regulations for the landing-takeoff (LTO) cycle up to 915 meters (3,000 feet) above airport runway on the emissions of NO_x, CO, unburned hydrocarbons, and smoke emissions [5][6][7]. During the LTO cycle, approximately 56% of all commercial aircraft emissions are in

the form of NO_x. Unburned hydrocarbons typically contribute less than 5%. Because of significant progress in combustor designs and improvement in specific fuel consumption, particulate matter emissions have been considerably reduced. As a result, NO_x releases below 3000 ft are currently a major emission concern around the airport. Incidentally, NO_x contributes to the reduction of methane in the upper troposphere, which is a positive effect [3]. Because engine thrusts are in general much higher during climb than during landing, the proper design of aircraft climb trajectories can be effective in reducing NO_x emissions at lower altitudes.

In addition to its own importance, the reduction of fuel burn directly reduces CO_2 emissions. The concentration of atmospheric greenhouse gases contributes to global warming. The world fleet releases approximately 13% of CO_2 emissions from all transportation sources, or 2% of all anthropogenic sources [8]. The expected doubling of the fleet over the next twenty years will certainly exacerbate the issue: the contribution of aviation is expected to increase by a factor of 1.6 to 10, depending on the fuel use scenario.

Importance of emissions impacts during cruise at high altitude

In the upper atmosphere, emissions released at high altitude are also recognized as an important issue with potentially severe long-term environmental consequences.

In addition to altering the concentrations of atmospheric greenhouse gases, aircraft emissions may trigger the formation of contrails, increase cirrus cover, and change other cloud properties. The energy and water budgets of the atmosphere are therefore affected and may contribute to climate change at the local and global scale.

At higher altitude, gases and particles emitted by aircraft during cruise accumulate in the atmosphere near the busiest flight routes, mainly in the northern mid-latitudes. Subsonic aircraft typically operate in the the region of the atmosphere that includes the upper troposphere, the tropopause, and the lower stratosphere. Because temperature is constant in the stratosphere regardless of altitude, there is no mechanism to drive emissions released in the lower stratosphere or tropopause to higher altitudes. Consequently, the residency time of the combustion products at these altitudes is high.

The direct impact of anthropogenic gases and particles on the climate is to change the absorption and scattering of radiation. Indirect effects that could potentially have

serious long-term consequences include chemical and physical changes of clouds and gases, essentially modifying the greenhouse properties of the atmosphere [8].

1.3.2 Computation of Aircraft Emissions

Emission NO_x

NO_x emissions are computed based on engine fuel flow (expressed in kg/s) and the combustor emission index (EI, expressed in g of NO_x formed per kg of jet fuel used) [9], both a strong function of power setting, during a take-off and landing cycle involving four different throttle modes: 100% (take off), 85% (climb), 30% (approach) and 7% (idle). Time in mode is simulated as follows: 0.7 minutes for take off, 2.2 minutes for climb, 4 minutes for approach, and 26 minutes for taxi/ground idle. The sum of the emissions at these four conditions (expressed in kg), calculated as shown in equation below, is used to determine the amount of NO_x emitted per LTO cycle.

$$\mathrm{NO_x} = \int_0^{TripTime} \text{Fuel Flow Rate} \times \mathrm{EI} dt \tag{1.1}$$

Other emissions: CO_2, H_2O, SO_2

During cruise, CO_2 emissions constitute 6% of the total mass flow emerging from the engine, versus 0.3% for NO_x and 0.04% for CO. Jet fuel provides the carbon required for the formation of CO_2, the hydrogen necessary for H_2O, and the sulfur for SO_2. As a result, by changing the amount of fuel required, aircraft can be configured to meet CO_2, H_2O, and SO_2 emissions requirements in addition to the NO_x emissions, cost, and noise constraints already discussed. CO_2, H_2O, and SO_2 trip emissions (in kg) are computed as shown in equation.

$$\text{Trip Emissions} = \text{Fuel Flow} \times \mathrm{EI} \times \text{Trip Time} \tag{1.2}$$

1.3.3 Current Ways to Reduce Environmental Impacts

Aircraft Design

The approach of optimizing aircraft design can give a better aircraft configurations to reduce fuel burn, emissions and noise. And there are several methods to do this: Improvements of combustor and engine circle; and better configuration of aircraft aerodynamics.

Current major way to reduce aircraft emissions is through better aircraft design. Commercial aircraft design processes have focused primarily on producing airplanes that meet performance goals at minimum operating costs. Environmental performance has been considered mostly at a post-design analysis phase, during which adjustments are made to satisfy the noise and emissions requirements of individual airlines or airports. The design parameters mainly include aerodynamics configurations and engine combustor condition.

Aircraft Operation

Another approach is from aircraft operation planning, using trajectory optimization method to plan aircraft trajectory for minimizing environmental problems. For this approach, optimal aircraft trajectory generation is an important role. With fixed aircraft design and configuration, an optimal aircraft trajectory is seeked for minimizing aircraft emissions or reducing aircraft noise. This thesis uses optimal trajectory planning method to reduce aircraft emissions during climb, because NO_x emission is released most when aircraft is climbing from take-off to cruise altitude.

1.4 Related Research

Many research efforts [10, 11, 12, 13, 14, 15, 16, 17, 18, 19, 20, 21, 22, 23] have been conducted on commercial aircraft trajectory planning and prediction that pave the ground for this work. In addition, classical aircraft performance studies [24, 25, 26, 27] examine steady-state climb and cruise flights with continuous variations of aircraft state. Optimal trajectory generations in this paper build on these excellent works and explicitly considered segmented flight structures in ATC. In addition, efforts are made for the

systematic evaluation of generated trajectories.

For surface flight management system, Gong [28] studied empirical kinematic trajectory models through regression analysis and data fitting. Capozzi et. al. [29] analyzed historical surface surveillance data in order to extract relations for kinematic motion model parameters across different portions of the airfield. Cheng and Sweriduk [30] examined trajectory design for aircraft taxi automation. Rentas, Green & Cate [31] illustrated the sensitivity of transit time predictions to the fidelity of trajectory modeling. Works have also been conducted for state estimations in the terminal and surface operations [32, 33]. Overall, however, the majority of existing literature focuses on the prediction and synthesis of airborne aircraft [23, 34, 35, 36, 37]. In comparison, direct work on surface-specific trajectory prediction and synthesis has been very limited.

In the past, effective departure and approach procedures have been studied for noise abatement [38, 39]. Optimization methods are also used to design departure and approach trajectories for noise abatement [40, 41, 42]. Recently, Torres & Chaptal [43] study the reduction of aircraft emissions and noise during the climb phase by optimizing departure procedures, using operational flight path software and a multi-mesh adaptive direct search method.

1.5 Organization of Thesis

The remainder of this thesis is organized into the following parts, chapters, and appendices.

- Part 1, including chapter 2, presents all required aircraft modeling work for flight trajectory generation, including aircraft equations of motion, motion constraints, aircraft performance model, and flight performance constraints.

- Part 2, including chapter 3 and 4, describes the ambient environmental modeling work for optimal trajectory planning to reduce environmental impacts of aircraft, including ambient environmental model, wind model, aircraft propulsion model, and emissions model.

- Part 3, including chapter 5, 6, 7, 8, and 9, first discusses systematic problem formulation of optimal trajectory planning and the solution methods. Chapter 6,

7, 8, and 9 generates optimal aircraft flights with respect to different performance indices, compares their differences and trade-offs, and examines different concepts of sensitivities.

- Appendix A gives all Glossary and Acronyms used in this thesis.
- Appendix B presents complete derivation of point-mass equations of motion for aircraft flight.
- Appendix C presents complete derivation of equations of motion for aircraft movement on surface.

Part I

Aircraft Models

Chapter 2

Modeling of Aircraft Flights

Trajectory analysis requires models of aircraft flights in the atmosphere that include equations of motion, motion constraints, aircraft performance, and atmosphere conditions. In addition, the ATC procedures specify structures of feasible flight trajectories.

2.1 Equations of Motion

Point-mass equations are typically adequate for subsonic commercial aircraft trajectory analysis. This thesis examines vertical flight trajectories where the lateral route is given. Flat earth and constant acceleration of gravity are assumed, and the mass is considered quasi-steady. For convenience of discussions, the resulting two-dimensional point-mass equations of motion in the vertical plane are listed below. The complete derivation of aircraft equations of motion is presented in Appendix B.

$$\dot{V}_t = \frac{T-D}{m} - g\sin\gamma_a - \dot{W}_s\cos\gamma_a - \dot{W}_h\sin\gamma_a \tag{2.1}$$

$$V_t\dot{\gamma}_a = \frac{L}{m} - g\cos\gamma_a + \dot{W}_s\sin\gamma_a - \dot{W}_n\cos\gamma_a \tag{2.2}$$

$$\dot{h} = V_t\sin\gamma_a + W_h \tag{2.3}$$

$$\dot{s} = V_t\cos\gamma_a + W_s = V_g \tag{2.4}$$

$$\dot{m} = -\frac{C_{tsfc}}{g}T \tag{2.5}$$

In these equations, lift and drag are given by

$$L = \frac{1}{2}\rho V_t^2 S C_L, D = \frac{1}{2}\rho V_t^2 S C_D \tag{2.6}$$

Flight trajectories are often expressed through Mach number, ground speed, Calibrated Airspeed (CAS), and/or pressure altitude. The Mach number is often defined as

$$M = \frac{V_t}{\sqrt{1.4R\Theta}} \tag{2.7}$$

and the ground speed can be determined from Eq. (6). For subsonic flights,

$$V_{CAS}^2 = 7R\Theta_{SL}\langle\{\bar{p}_h[(0.2M^2+1)^{3.5}-1]+1\}^{\frac{2}{7}}-1\rangle \tag{2.8}$$

Finally, throttle setting defined as the percentage of the total thrust employed is often used as a trajectory control variable in place of the thrust.

$$\kappa = \frac{T - T_{min}}{T_{max} - T_{min}} \tag{2.9}$$

The above equations have five trajectory state variables V_t, γ, h, m, four output variables: M, V_{CAS}, V_g, h_p , and two trajectory control variables: T, C_L.

2.2 Motion Constraints

Motion constraints define a flight envelope in which an aircraft must operate. For commercial aircraft, the flight path angle is constrained by both aircraft performance capabilities and passenger comfort. Airspeed must stay above its stall limit and below the maximum operating speed (VMO) for structural integrity. In addition, the Mach number usually stays below its drag divergence value, which is often more limiting than the not-to-exceed airspeed. We have

$$\gamma_{min} \le \gamma \le \gamma_{max},\ V_t \ge V_{min} = 1.2\sqrt{\frac{2W}{\rho S C_{L_{max}}}},\ M \le M_{max} \tag{2.10}$$

where a 20% margin included in the stall speed.

In addition, current ATC regulations specify that CAS cannot exceed 250 knots when the aircraft is below 10,000 ft.

$$V_{CAS} \leq 250kts, \text{for } h \leq 10,000ft \tag{2.11}$$

Other constraints on trajectory variables include

$$C_{L_{min}} \leq C_L \leq C_{L_{max}},\ T_{min} \leq T \leq T_{max} \text{ or } 0 \leq \kappa \leq 1 \tag{2.12}$$

The load factor constraint can be expressed

$$n = \frac{L}{W} = \frac{\rho V_t^2 S}{2W} C_L \leq n_{max} \tag{2.13}$$

For supersonic aircraft, there may also be a maximum heating constraint. This is often not an issue for subsonic vehicles.

Finally, aircraft altitude is constrained by the ceiling altitude and a minimum altitude

$$h_{min} \leq h \leq h_{max} \tag{2.14}$$

where the ceiling altitude is a function of maximum thrust available.

2.3 Aircraft Performance Model

To obtain numerical solutions, a generic transport aircraft similar to Airbus 320 is assumed, which has a gross weight in the order of $m_0 = 141,100lbm$, $S_{surf} = 1320ft^2$, $c_{tsfc} = 0.75lbm/(lbf - hr)$, $h_{max} = 41kft$, $\gamma_{max} = 8^0$, $\gamma_{min} = -3^0$, $n_{max} = 1.2$, $M_{max} = 0.82$, VMO $= 350kts$. The above values can be obtained from Base of Aircraft Data (BADA) Revision 3.9.

2.3.1 Aircraft Aerodynamic Model

Both the lift coefficients and drag coefficients are functions of the angle of attack, thus the drag coefficient can interpreted that it depends on the lift coefficient. The drag coefficient related to the lift coefficient is called the "drag polar" of the aircraft [24].

The drag coefficient never becomes zero, and can be divided into two components

$$C_D = C_{D_{min}}(M, Re) + C_{D_i} \tag{2.15}$$

The minimum drag coefficient $C_{D_{min}}$ is called the parasite drag coefficient, and depends on the Mach number (M), the Reynolds number (Re) and the aircraft configuration. C_{D_i} is called the induced drag coefficient and depends on the lift coefficient.

$$C_{D_i} = K(M, Re)(C_L - C_{L_0})^2 \tag{2.16}$$

where K is dependent on the aircraft wing dimensions, the Mach number (M), the Reynolds number (Re) and the aircraft configuration. C_{L_0} is the lift coefficient at zero angle of attack. Therefore the drag polar of a modern cambered wing transport aircraft can be represented with

$$C_D = C_{D_{min}}(M, Re) + K(M, Re)(C_L - C_{L_0})^2 \tag{2.17}$$

For the aircraft with symmetrical wing sections, the drag polar

$$C_D = C_{D_0}(M, Re) + K(M, Re)C_L^2 \tag{2.18}$$

where C_{D_0} is the zero-lift drag coefficient. Because of the simplicity of the drag polar equation given by equation, sometimes this representation is sued even for performance analysis of the cambered wing aircraft [24].

The change in the Reynolds number has only a small effect on the value of C_D. If the Reynolds number which is selected for the computation is around the lowest value expected to be experienced in flight, the drag coefficient will be on the conservative side (slightly higher). Hence, if the effects of Reynolds number changes are neglected, the functional relation for the drag coefficient becomes [26]

$$C_D = C_{D_0}(M) + K(M)C_L^2 \tag{2.19}$$

In this thesis, values of zero-lift drag coefficient C_{D_0} and induced drag drag coefficient K are selected as constant for different phases of flight, including initial climb, take-off, cruise, approach, and landing. The values can be obtained from BADA 3.9.

2.3.2 Aircraft Propulsion Model

The propulsion model defines the thrust available and the specific fuel consumption.

Thrust

The nominal climb thrust limits for turbojet engine is provided by [44]

$$T_{max} = C_{T1} \times (1 - \frac{H_p}{C_{T2}} + C_{T3} \times H_p^2) \tag{2.20}$$

The cruise and descent thrust limits are corrected by factors

$$T_{max,cr} = C_{Tcr} \times T_{max} \tag{2.21}$$

$$T_{max,des} = C_{Tdes} \times T_{max} \tag{2.22}$$

The cruise and descent thrust limits are corrected by factors [45, 12]

$$T_{max,ap} = C_{Tap} \times T_{max} \tag{2.23}$$

$$T_{max,ld} = C_{Tld} \times T_{max} \tag{2.24}$$

Where coefficients C_{T1}, C_{T2}, C_{T3}, and factors C_{Tcr}, C_{Tdes}, C_{Tap}, C_{Tld} can be obtained from BADA 3.9.

Specific-fuel consumption

For the specific fuel consumption the following general model is considered [44]

$$c = C_{f1} \times (1 + \frac{V_t}{C_{f2}}) \tag{2.25}$$

The nominal fuel flow is computed by

$$f_{nom} = c \times T \tag{2.26}$$

For descent phase where sometimes aircraft is operated at idle thrust, the fuel flow has a low limit, so the descent fuel flow rate has to be the maximum value of nominal fuel flow and minimum limit,

$$f_{des} = max[f_{nom}, f_{min}] \tag{2.27}$$

where the minimum fuel flow is computed by

$$f_{min} = C_{f3} \times (1 - \frac{H_p}{C_{f4}}) \tag{2.28}$$

During cruise phase, the fuel flow rate needs to be corrected by a factor

$$f_{cr} = f_{nom} \times C_{fcr} \tag{2.29}$$

Where all fuel flow rate factors can be obtained from BADA 3.9.

Part II

Environmental Models

Chapter 3

Ambient Atmospheric Model

3.1 Models of Ambient Pressure, Density, and Temperature

To make the aircraft equations of motion complete, models of ambient pressure, density, and temperature are needed. International Standard Atmosphere (ISA) defines pressure, density, and temperature as functions of geometric altitude, denoted as $p_{ISA}(h)$,$\Theta_{ISA}(h)$,$\rho_{ISA}(h)$. These expressions can be derived from three relations: the perfect gas law, the hydrostatic equation, and a temperature profile based on measurements [27]. Specifically, the altitude range of commercial subsonic flights can be divided into two temperature regions: the gradient region from sea level to the tropopause in which the temperature decreases linearly as altitude increases, and the isothermal region above the tropopause in which the temperature stays constant. For the convenience of discussions, the standard atmosphere expressions are summarized below.

for $h \leq h_T$

$$\Theta_{ISA}(h) = \Theta_{SL} + l_a h \tag{3.1}$$

$$\frac{p_{ISA}(h)}{p_{SL}} = (1 + \frac{l_a}{\Theta_{SL}} h)^{-\frac{g}{l_a R}} \tag{3.2}$$

$$\frac{\rho_{ISA}(h)}{\rho_{SL}} = (1 + \frac{l_a}{\Theta_{SL}} h)^{-\frac{g}{l_a R}-1} \tag{3.3}$$

and for $h_T \leq h \leq h_2$

$$\Theta_{ISA}(h) = \Theta_T \tag{3.4}$$

$$\frac{p_{ISA}(h)}{p_{SL}} = \frac{p_T}{p_{SL}} e^{-\frac{g}{R\Theta_T}(h-h_T)} \tag{3.5}$$

$$\frac{\rho_{ISA}(h)}{\rho_{SL}} = \frac{\Theta_T}{\Theta_{SL}}^{-\frac{g}{l_a R}-1} e^{-\frac{g}{R\Theta_T}(h-h_T)} \tag{3.6}$$

where h_T is the beginning altitude of the isothermal region, (p_T, Θ_T) are the (pressure, temperature) in the isothermal region, and l_a is the temperature lapse rate in the lower gradient region. Standard values are given by: $\Theta_{SL} = 288.16K = 518.69^oR$, $p_{SL} = 1.01325 \times 10^5 N/m^2 = 2,116.2lb/ft^2$, $\rho_{SL} = 1.225kg/m^3 = 0.002377slug/ft^3$, $R = 287j/(kgK) = 1716(lbft)/(slug^oR)$, $l_a = -0.0065K/m = -0.00356^oR/ft$, $h_T = 36,089ft = 11km$, $h_2 = 82,020ft = 25km$, $\Theta_T = 216.66K$, and $p_T = 0.22336p_{SL}$.

Accordingly, pressure altitude can be determined from.

$$h_p(p) \quad = \frac{\Theta_{SL}}{l_a}[(\frac{p}{p_{SL}})^{-\frac{l_a R}{g}} - 1] \text{ for } p \geq p_T \tag{3.7}$$

$$h_p(p) \quad = h_T + \frac{R\Theta_T}{g}\ln(\frac{p_T}{p}) \text{ for } p \leq p_T \tag{3.8}$$

Pressure altitudes are often stated as Flight Levels (FLs). For example, FL 300 corresponds to a pressure altitude of 30 kft.

Furthermore, baro-corrected altitude h_b can be obtained by replacing the standard sea-level pressure in Eq. (3.7) with the altimeter reading from a given airport. Clearly, barometric altitude gives more accurate indication of the altitude with respect to the ground. As a result, barometric altitude is used during takeoff and landing, whereas pressure altitude is used during cruise flight. In the United States, pressure altitude is used after a climbing aircraft passes 18 kft of barometric altitude. Conversely, barometric altitude is used for an aircraft on approach when the pressure altitude drops below FL180.

3.2 Models of Wind

Actual wind velocities can vary with location, altitude, and the time of the year. They contain both relatively steady and time-varying components. In this study, we seek to

examine the effects of the general wind patterns as well as wind measurement accuracies on optimal trajectory planning and prediction. To this end, a model of the average wind profile as a function of altitude is used. Typically, the mean wind speed gradually increases as altitude increases and reaches a peak in the jet-stream altitude range of 10-15 km. As the altitude increases further, it gradually decreases to reach a minimum around 18- 25 km. Figure 3.1 shows wind profiles for the east-west and the north-south components. This is representative of the typical wind profiles observed in the continental U.S. A representative average horizontal wind speed profile is shown in Fig. 3.1 .In this study, the nominal vertical wind is assumed zero.

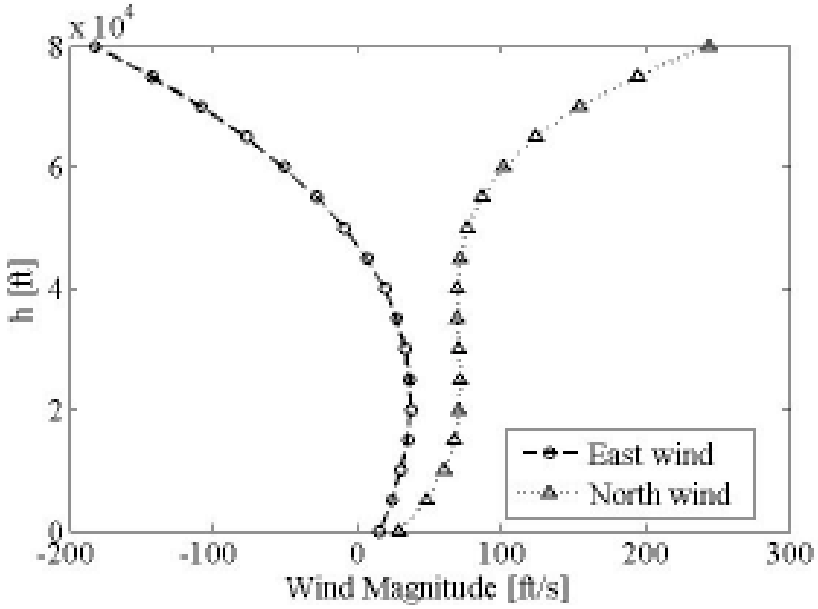

Figure 3.1: A representative horizontal wind profile in continental US.

Once the wind components along north and east are known, the horizontal wind along a specified flight path $\Psi_c(s)$ can be determined from

$$W_s = W_e \sin \Psi_c + W_n \cos \Psi_c \tag{3.9}$$

Chapter 4

Modeling of Aircraft Emissions

4.1 Products of Emissions

Aircraft emissions come from combustion process within burner of aircraft engines. Both particulate and gaseous pollutants are produced through the combustion of jet kerosene. For kerosene fuel, the reactants and products of combustion process are:

Reactants: Air $N_2 + O_2$ and Fuel $C_nH_m + S$

Products: $CO_2 + H_2O + N_2 + O_2 + NO_x + UHC + CO + C_{soot} + SO_x$

The greenhouse gases are carbon dioxide CO_2 and water H_2O. Pollutant emissions formed during combustion include nitrous oxides NO_x, unburned hydrocarbons UHC, carbon monoxide CO, and soot C_{soot}.

Aviation emissions strongly affect air quality in the vicinity of airports [7]. Accordingly, the International Civil Aviation Organization (ICAO) has regulations for the landing-takeoff (LTO) cycle up to 915 meters (3,000 feet) above airport runway on the emissions of NO_x, CO, unburned hydrocarbons, and smoke emissions [6]. During a LTO cycle, about 56% of all commercial aircraft emissions are in the form of NO_x. Unburned hydrocarbons typically contribute less than 5%. In addition, particulate matter emissions have been considerably reduced; thanks to the significant progress in combustor designs and improvement in specific fuel consumption. As a result, NOx releases below 3000 ft represent a major emissions concern around the airport. Incidentally, NOx contributes to the reduction of methane in the upper troposphere, which is a positive effect [3].

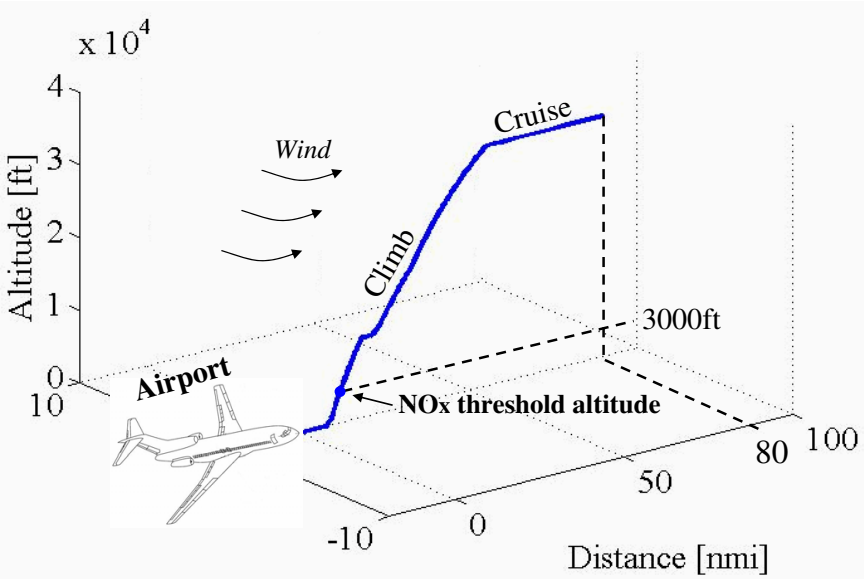

Figure 4.1: Effective altitudes for NO_x emissions reduction.

This thesis studies the reduction of NO_x below 3,000 ft and CO_2 throughout climb and descent, as illustrated in Fig. 4.1. Generally, aircraft emissions can be computed by integrating the product of engine fuel flow rate and the combustor emissions index (EI), which is measured in weight of emissions per unit weight of fuel burned. When the fuel flow rate is expressed in kg/s and EI in g per kg of fuel used, the emissions are measured in term of g. Different emissions component may have different EI.

4.2 Emissions Modeling

4.2.1 Prediction of NO_x

The NO_x formation and destruction process predominantly takes place in the post-flame gases, through chemical reactions involving nitrogen and oxygen atoms and molecules that do not attain chemical equilibrium [9]. As the burned gases cool, the reactions involving NO_x freeze and leave concentrations that exceed the levels that would correspond to equilibrium at combustor exhaust.

Because NO_x formation is mostly a function of equivalence ratio and combustion temperature, obtaining this data requires detailed modeling of the combustion process.

A conventional approach for estimating NO_x is the "P3T3" method, which was developed as part of the NASA Glenn Advanced Subsonic Technology project, based on internal NASA data, models from industry, and estimates of the NO_x emissions index [46]. Knowledge of the flow conditions at the combustor entry and outlet are required. The correlation for the NO_x emissions index (g/kg) is given by

$$\mathrm{EI}_{\mathrm{NO_x}} = 0.004194\Theta_{T4}(\frac{P_{T3}}{439})^{0.37}e^{\frac{\Theta_{T3}-1471}{345}} \tag{4.1}$$

where P_{T3} is the total pressure at the combustor entry in psia, and (Θ_{T3}, Θ_{T4}) are the total temperature at the combustor entry and outlet in Rankine, respectively.

This "P3T3" method relies on proprietary aircraft and engine manufacturer information, which is hard to measure and to obtain. As a result, a more transparent method called "Fuel Flow Method 2" was developed [47]. This model requires information of current ambient temperature and pressure, current engine fuel flow, and engine emissions indices data at LTO cycles, all of which are fairly readily available from ICAO data bank.

Specifically, with the knowledge of the current fuel flow at a given altitude, the corresponding fuel flow at sea level can be computed from

$$W_{f,SL} = W_{f,alt}(\frac{\Theta_{amb}^{3.8}}{\delta_{amb}})e^{0.2M^2} \tag{4.2}$$

Where, Θ_{amb} and δ_{amb} can be computed from current ambient pressure and temperature

$$\Theta_{amb} = \theta_{amb}/518.67 \tag{4.3}$$

$$\delta_{amb} = p_{amb}/14.696 \tag{4.4}$$

Then, the sea level $EI_{NO,SL}$ can be determined from the ICAO engine emissions data bank [48] that corresponds to $W_{f,SL}$. The emissions index at the current altitude can then be calculated from

$$\mathrm{EI}_{\mathrm{NO_x}} = \mathrm{EI}_{\mathrm{NO_x},SL}(\frac{\delta_{amb}^{1.02}}{\Theta_{amb}^{3.3}})^{0.5}e^{H} \tag{4.5}$$

Where, H is computed from

$$\Theta_{ambc} = \frac{\Theta_{amb}}{1.8} - 273.15 \tag{4.6}$$

$$p_{sat} = 6.107 \times 10^{\frac{7.5\times\Theta_{ambc}}{237.3+\Theta_{ambc}}} \tag{4.7}$$

$$\omega = \frac{0.62197058\times\phi\times p_{sat}}{P_{amb}\times 68.9473 - \phi\times p_{sat}} \tag{4.8}$$

$$H = -19(\omega - 0.00634) \tag{4.9}$$

Finally, the total NO_x emissions over a certain time window $[t_0, t_1]$ can be computed from

$$NO_x = \int_{t_0}^{t_f} EI_{NO_x} * \dot{W}_f dt \tag{4.10}$$

In this paper, the relative humidity is assumed to be $\phi = 40\%$. An Airbus 320 aircraft is used as a reference, and the corresponding engine model is CFM56-5B4. Table 4.1 gives the performance data of the CFM56-5B4 engine published by ICAO [48]. Based on the ICAO data, a polynomial fitting of the relationship between the emissions index of NOx at sea level and the engine fuel flow rate is obtained as

$$EI_{NO_x} = 11.6864\dot{W}_{f,SL}^3 - 22.2423\dot{W}_{f,SL}^2 + 33.8749\dot{W}_{f,SL} + 0.9157 \tag{4.11}$$

Table 4.1: Measured data of Emission Index for engine CFM56-5B4.

Mode	Power Setting	EI_{HC}(g/kg)	EI_{CO}(g/kg)	EI_{NO_x}(g/kg)
Take-off	100%	0.1	0.5	28.7
Climb out	85%	0.1	0.5	23.3
Approach	30%	0.13	2.33	10
Idle	7%	3.87	31.9	4.3

where, EI_{NO_x} is in g/kg, $\dot{W}_{f,SL}$ is the corresponding fuel flow at sea level, in kg/s.

4.2.2 Prediction of other fuel proportional emissions

Unlike emission NO_x, the production of CO_2, H_2O, and SO_2 species production is directly proportional to the fuel burnt, modeling these emissions only requires knowledge of fuel consumption and fuel-specific emission indices. For jet kerosene, the emission indices are shown in Table 4.2.

Table 4.2: Emissions Index (EI) of species proportional to fuel consumption.

Emissions	EI(g/kg fuel)
CO_2	3,155
H_2O	1,240
SO_2	0.8

Therefore, in this thesis, the production of CO_2 (in kg) is computed by

$$CO_2 = \mathrm{EI}_{CO_2} \times W_f \tag{4.12}$$

Part III

Optimal Flight Trajectories Planning

Chapter 5

Mathematical Formulation and Solution Methods

Following the typical flight trajectory procedure, the trajectory planning process can be formulated as a mathematical problem. In today's ATC procedures, a complete commercial flight trajectory typically consists of three phases: climb, cruise, and descent (Fig. 5.1). Each phase is in turn composed of a series of flight segments, where each segment is characterized by a set of flight objectives. In addition, a series of selected flight segments constitute a trajectory profile. Studies of trajectory planning and prediction in ATC should consider the trajectory structures imposed by these segments and profiles. As a result, the mathematical representations of these flight segments and profiles are needed.

5.1 Typical Structure of Aircraft Flight Trajectory

For a high-speed subsonic commercial transport, representative segments during the climb phase include constant Mach/CAS climb with a constant throttle setting, climb with specified acceleration and throttle setting, and level flight with specified acceleration or throttle setting. Descent flight segments are similar in structure to those of the climb phase. In comparison, the cruise phase can be characterized by segments of level flight with a specified Mach or true airspeed, or cruise climb with constant speed and constant lift coefficient. Summarizing these different cases, a generic vertical flight

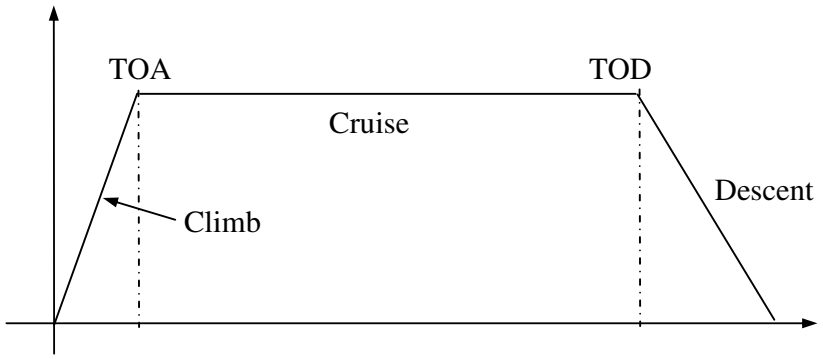

Figure 5.1: A complete vertical trajectory from liftoff to touchdown

segment can be described by specifying two objectives out of the five variable groups that use different trajectory controls [49], presented in Table 5.1. Then, a trajectory profile can be defined as an ordered sequence of selected flight segments.

Table 5.1: Mathematical description of flight segments.

Variable Group	Choices	Control	Orders
Speed	M, V_{CAS}, orV_t	T or C_L	1^{st} using T, 2^{nd} using C_L
Accel/Decel	$\dot{V}_t$	T	0^{th}
Throttle	κ	T	0^{th}
Altitude	h_p, $\dot{h}$, or γ	C_L	2^{nd} for h_p, 1^{st} for $\dot{h}/\gamma$
Lift Coefficient	C_L	C_L	0^{th}

In connecting two segments in a profile, a certain monotonic variable during the first segment is defined as a capture variable [49]. When this variable reaches a specified threshold, the second segment begins. The definition of a trajectory profile needs to specify the sequence of segments as well as the capture conditions to connect them.

5.2 Models of Closed-Loop Trajectory Tracking

In actual flights, pilots or autopilots actively follow the objectives of the segments in the presence of disturbances. Actual logics of closed-loop tracking can be very complicated. In this paper, the method of feedback linearization29 is used to model the essential logics of closed-loop tracking. In this method, the difference between a specified flight objective

and its measured value is regulated. In applying feedback linearization, this difference (tracking error) is differentiated until a selected trajectory control variable appears. The required number of differentiations is called the order of the flight objective using the specified control. Then, the desired closed-loop response dynamics is specified by selecting the closed-loop gains to model reasonable pilot or autopilot responses.

For example in a level flight, airspeed is controlled with thrust whereas altitude is controlled with the lift coefficient (or pitch). The airspeed objective using thrust control is of first-order, and a desired tracking dynamics may be specified as

$$\dot{V}_t + K_{Vt}(\hat{V}_t - V_c) = 0 \tag{5.1}$$

where $K_{Vt} > 0$ is the control gain. In comparison, the altitude objective with lift control is of second-order, and a desired tracking dynamics may be specified as

$$\ddot{h}_p + 2\zeta_h \omega_h \hat{\dot{h}}_p + \omega_h^2 (h_p - h_{p,c}) = 0 \tag{5.2}$$

where $\omega_h > 0$ is the natural frequency, and ζ_h is the damping ratio. Typical human pilot responses would correspond to $K_V = 0.05 \sim 0.1$, $\zeta \approx 0.5 \sim 0.7$, and $\omega_h \approx 0.05 \sim 0.5$. Closed-loop trajectory tracking laws for other segments can be similarly obtained.

In general, the order of a flight objective depends on both the objective itself and the control variable. For example, airspeed controlled with thrust is of first-order (speed-on-throttle). In comparison, airspeed controlled with lift coefficient becomes second-order (speed-on-pitch). Table 5.1 shows the guidance law orders of typical flight segments.

5.2.1 Models of Pilot Control Actions

In flights, pilots or autopilots actively seek to track trajectory intents in the presence of disturbances. Even with the use of the same guidance strategies, different pilots may apply control actions differently to follow these intents. Models are needed to describe individual pilot control actions.

Mathematical descriptions of human operators through dynamic response models fall into the research field of manual control [50, 51]. In particular, the control-theoretic representation has become the fundamental model of the human operator in manual

control. Research on automobile controls also provides useful references for the modeling of pilot control actions during surface movements [52, 53, 54].

With the increasing automation in airplane cockpits, the role of a human pilot is changing from that of a continuous controller to that of a supervisor or manager. As of now, human performance modeling in aviation is able to represent relatively complex aircraft-ATC interactions with sufficient realism [55, 56]. For use in trajectory planning and prediction, on the other hand, manual control models are often adequate.

A typical model structure of pilot control actions based on manual control is shown in Fig. 5.2. First, differences between intents and relevant aircraft states are measured. These differences are displayed to the pilot. Both the display and the pilot observation process incur errors, and these errors may be modeled as random variables. Next, the pilot applies appropriate control actions, after some reaction delay, to zero out the differences between the intents and displayed states in a closed-loop tracking, which is modeled with the method of feedback linearization discussed below. Finally, the neuro-muscular behavior of the human pilot affects the implemented control actions. This effect is typically modeled as a first-order delay. For trajectory planning, one may ignore pilot reaction delays and the neuro-muscular effects. For trajectory predictions, on the other hand, it may be beneficial to include them in order to understand likely prediction errors.

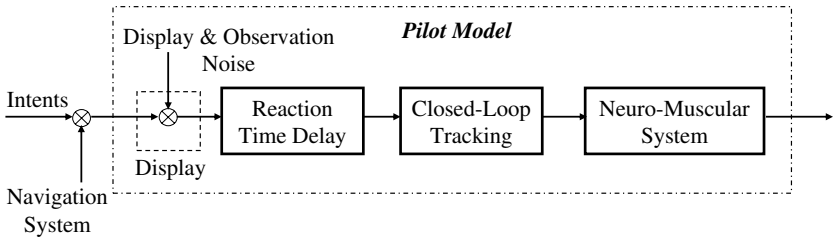

Figure 5.2: Components of a pilot model.

5.3 The Assumption of Perfect Trajectory Tracking

Perfect tracking is an idealization that pilots and/or autopilots follow flight objectives precisely. This assumption makes it possible to replace some differential equations with

algebraic equations and thus reduce computational loads. It has been implicitly assumed in most of the current algorithms for trajectory planning and predictions [22, 23]. This assumption makes it possible to replace some differential equations with algebraic equations. For example, a perfectly tracked constant Mach segment completely specifies the true airspeed through Eq. (2.7). As a result, it is no longer necessary to integrate Eq. (2.1). Because perfect tracking assumes that an aircraft can meet the flight objectives of a subsequent segment instantaneously, it can result in jumps in some trajectory variables across connecting segments. Still, it is found that overall differences caused by the perfect tracking assumption are negligible in generating nominal trajectories.

In this thesis, perfect tracking is assumed in the generation of optimal nominal trajectories. In evaluating sensitivities of optimized trajectories in actual flights, on the other hand, closed-loop trajectory tracking is used.

Chapter 6

Optimal Climb Flights

Aircraft climb flights in the ATC system are now formulated as parameter optimal control, in which, flight segment parameters are determined to minimize NO_x, fuel consumption (equivalently CO_2), flight time, distance traveled, or their combinations.

6.1 Formulation of Optimal Climb Trajectory Planning

Fig. 6.1 below shows a representative climb profile that consists of a series of flight segments from liftoff to cruise. Table. 6.1 defines these segments in the climb profile and the corresponding capture conditions.

Table 6.1: Segments and capture conditions in a representative climb profile.

No.	Segment Type	Flight Objectives	Capture Condition
C0	Ground Run and Initial Climb	κ_c, C_{L_c}	Reaching 50 ft
C1	Climb with Acceleration	$\dot{V}_{t,c}$, $\dot{h}_{p,c}$	Reaching a CAS
C2	Climb with Constant CAS	$V_{CAS,c}$, κ_c	Reaching an Altitude
C3	Level Acceleration	$\dot{V}_{t,c}$, $h_{p,c}$	Reaching a CAS
C4	Climb with Constant CAS	$V_{CAS,c}$, κ_c	Reaching a Mach
C5	Climb with Constant Mach	M_c, κ_c	Reaching an Altitude

There are in general four fundamental considerations in the climb phase: the time required, the amount of fuel consumed (equivalently CO_2), emission NO_x, and/or horizontal distance traveled for an aircraft to reach a specified cruise altitude. Correspondingly for optimal planning of climb trajectories in an ATC environment, flight objectives

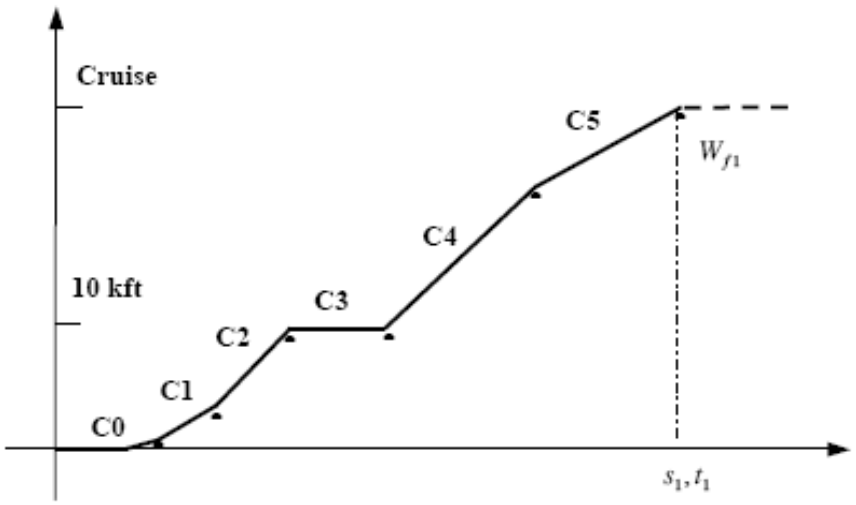

Figure 6.1: A representative climb trajectory

of the constituting segments can be selected to minimize the flight time, fuel consumption, emission NOx, or distance traveled, or their appropriate combinations, subject to the requirement that the aircraft reaches a specified cruising altitude at the end of the climb phase, Fig. 6.2. A minimum-time clime would enable the aircraft to reach the cruise level in the shortest possible time. A minimum-fuel climb represents the most economical climb out of a terminal area. Finally, a minimum-distance climb enables the aircraft to clear out of vertical obstacles quickly.

These problems can be stated mathematically. Denoting climb flight objectives of different segments in the flight profile as p_{ck} , $k = 1, 2, ..., N_c$, where N_c is the total number of objectives in each segment during climb, and

$$p_{ck,min} \leq p_{ck} \leq p_{ck,max} \tag{6.1}$$

where constraints on each flight objective come from the motion constraints discussed above, the climb phase decision parameter vector can then be expressed as

$$\vec{p_c} = [p_{c1}, p_{c2}, ..., p_{cN}] \tag{6.2}$$

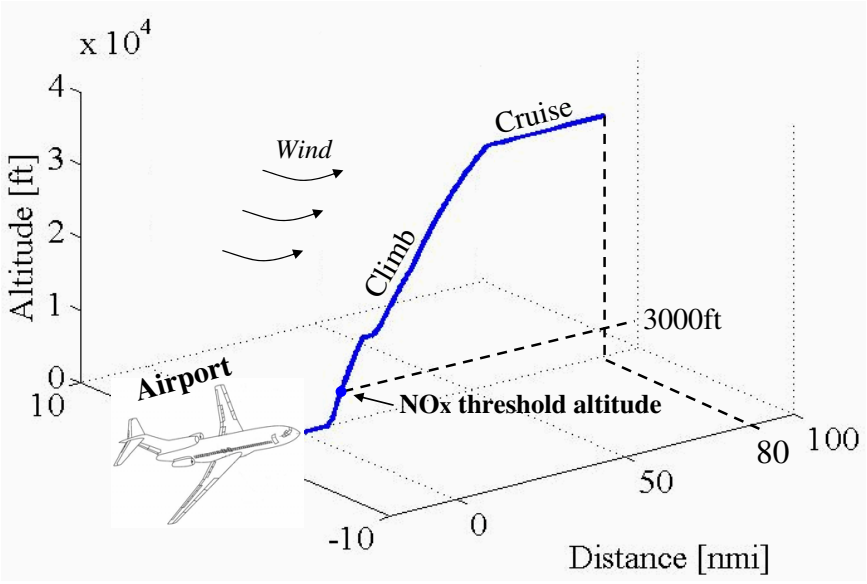

Figure 6.2: Effective altitudes for NO_x emissions reduction.

An optimal climb flight can be formulated to minimize the performance index

$$\min_{\vec{p}_c} I(\vec{p}_c) = K_f \Delta W_{f,c} + K_t t_{f,c} + K_{\mathrm{NO_x}} W_{\mathrm{NO_x},c} + K_s s_c \tag{6.3}$$

subject to Eqs. (2.1)-(2.5), and appropriate initial conditions

$$V_{t_0} = V_0, \gamma_{t_0} = 0, h_{t_0} = h_0, s_{t_0} = 0, m_{t_0} = W_0/g \tag{6.4}$$

parameters bounded in Eq. (6.1), and the terminal constraint that the aircraft reaches a specified cruise altitude and a specific cruise Mach number,

$$h(t_f) = h_{cr}, M(t_c) = M_{cr}, \gamma_a(t_c) = 0 \tag{6.5}$$

In some optimization studies, the total climb distance is specified: $s(t_c) = s_c$. In this study, it is assumed $h_{cr} = 33000$ft, $M_{cr} = 0.82$, and when applicable $s_c = 80$nmi.

In Eq. (6.3), $K_f, K_t, K_{\mathrm{NO_x}}, K_s$ are weighting factors. By setting these weights properly, both "single-criterion" and combined optimal trajectories can be obtained. For example, a minimum-fuel climb trajectory results by setting $K_f = 1$ and the rest to zero.

In the above problem, the fuel consumption during climb is calculated as

$$W_{f,c} = [m(t_0) - m(t_c)]g \tag{6.6}$$

and the NO_x emissions up to the threshold altitude of 3000ft are calculated from

$$W_{\mathrm{NO_x},c} = \int_{t_0}^{t_1} \mathrm{EI}_{\mathrm{NO_x}} \cdot \dot{W}_f dt \tag{6.7}$$

where $h(t_1) = 3000$ft, and $\dot{W}_f = c_{tsfc}T$.

6.2 Numerical Solution Methods

The above problems constitute a parameter optimal control of dynamical systems with terminal constraints and control parameter bounds. Typically, nonlinear optimal control problems can be converted into parameter optimization by discretizing the time interval and then representing trajectory state and/or control variables by their respective values at the series of time points [57, 58, 59, 60, 61]. However, the conventional discretization approach would require considerable bookkeeping to solve the current problem because different segments may have different equations and switching times between adjacent segments are changing in the optimization process.

In this study, a gradient algorithm is devised and presented below. This algorithm takes an initial trajectory guess and iteratively calculates optimal segmented trajectories. It obtains accurate numerical solutions for optimal trajectory generations in ATC. For this reason, it can be used to assess any other approximate solution schemes. This algorithm is used to solve all the trajectory optimization problems in this study.

A generic trajectory generation problem is a parameter optimal control that seeks to determine optimal parameter values by minimizing a scalar cost. A gradient algorithm is used. This algorithm takes an initial trajectory guess and iteratively improves performances of the segmented trajectories. Specifically, the above parameter optimal control problems seek to determine optimal decision parameters by minimizing a scalar cost.

$$\underset{\vec{p}\in P}{I} = I(\vec{p}) \tag{6.8}$$

subject to a terminal constraint

$$\vec{\varphi}(\vec{p}) = 0 \tag{6.9}$$

where

$$\vec{p} = [p_1, ..., p_m]^T, p_{k,min} \leq p_k \leq p_{k,max} k = 1, ..., m \tag{6.10}$$

Denoting

$$I_p = (\frac{\partial I}{\partial \vec{p}})_{\vec{p}^0} \in R^{l \times m} \tag{6.11}$$

$$\vec{\varphi}_p = (\frac{\partial \vec{\varphi}}{\partial \vec{p}})_{\vec{p}^0} \in R^{r \times m} \tag{6.12}$$

$$\vec{\varphi}^0 = \vec{\varphi}(\vec{p}^0) \in R^r \tag{6.13}$$

an iterative gradient method is devised as follows.

Starting with some initial guess of the parameter $\vec{p}^0$, an update $\Delta\vec{p}$ is sought so that

$$\Delta I \approx I_p \Delta\vec{p} \leq 0 \tag{6.14}$$

and

$$\vec{\varphi}(\vec{p}^0 + \Delta\vec{p}) \approx \vec{\varphi}(\vec{p}^0) + \vec{\varphi}_p \Delta\vec{p} = (1 - \varepsilon)\vec{\varphi}(\vec{p}^0) \tag{6.15}$$

or

$$\vec{\varphi}_p \Delta\vec{p} = -\varepsilon\vec{\varphi}^0 \tag{6.16}$$

where $0 \leq \varepsilon \leq 1$ is a stepsize in improving the terminal constraint

The parameter update can be selected as

$$\Delta\vec{p} = -\beta(I_p + \vec{v}^T\vec{\varphi}_p)^T = -\beta(I_p^T + \vec{\varphi}^T\vec{v}) \tag{6.17}$$

Where $\beta > 0$ is a stepsize and $\vec{v} \in R^r$ is a Lagrange multiplier vector. Substituting Eq. (65) into Eq. (64) leads to

$$\vec{v} = (\vec{\varphi}_p\vec{\varphi}_p^T)^{-1}(\frac{\upsilon}{\beta}\vec{\varphi}^0 - \vec{\varphi}_p I_p^T) \tag{6.18}$$

The corresponding first-order change in the cost function is

$$\Delta I = -\upsilon I_p \vec{\varphi}_p^T (\vec{\varphi}_p \vec{\varphi}_p^T)^{-1} \vec{\varphi}^0 - \beta [I_p I_p^T - I_p \vec{\varphi}_p^T (\vec{\varphi}_p \vec{\varphi}_p^T)^{-1} \vec{\varphi}_p I_p^T] \tag{6.19}$$

For a sufficiently small ϵ, the incremental cost function in Eq. (6.19) is is guaranteed to decrease. The stepsize υ should also be small to ensure the validity of the linear approximation in Eqs. (6.14) and (6.15).

In this paper, a forward difference scheme is used to calculate gradients numerically. The bounds on optimization parameters in Eq. (6.10) are applied at each iteration step. Because of the bounds on the optimization parameters in Eq. (6.10), the gradient of the cost function with respect to the optimization parameters may not necessarily be small at convergence if their optimal values occur on bounds. As a result, the norm of the gradient may not be a good stopping criterion. Instead, iterations are terminated when both the magnitude of the terminal constraint and the relative improvement in the cost function become sufficiently small. The program may also be terminated if the maximum number of iterations is reached.

If the terminal constraint in Eq. (6.9) is removed, the parameter update is simply

$$\Delta \vec{p} = -\beta I_p^T \tag{6.20}$$

and the Lagrange multiplier vector is not used. In both cases, the bounds on parameters in Eq. (6.10) are applied at each iteration step.

6.3 Calculated Optimal Climb Trajectories

Fig. 6.3 and Fig. 6.4 show four optimal climb trajectories, where each optimizes one criterion separately. Table 6.2 presents the fuel consumption, flight time, distance traveled, and NO_x emissions below 3,000 ft for the four single-criterion optimal climb trajectories. In general, the four different performance criteria produce different trajectories.

Specifically, the minimum-distance trajectory gives the steepest climb profile of all, as expected. The minimum-fuel and minimum-time trajectory are in the middle. And the corresponding fuel burn and climb time of minimum-fuel and minimum-time trajectories are close, as shown in Table 6.2. This is consistent with the steady-state analysis of unconstrained flights, where the minimum-time and minimum-fuel climb flights are

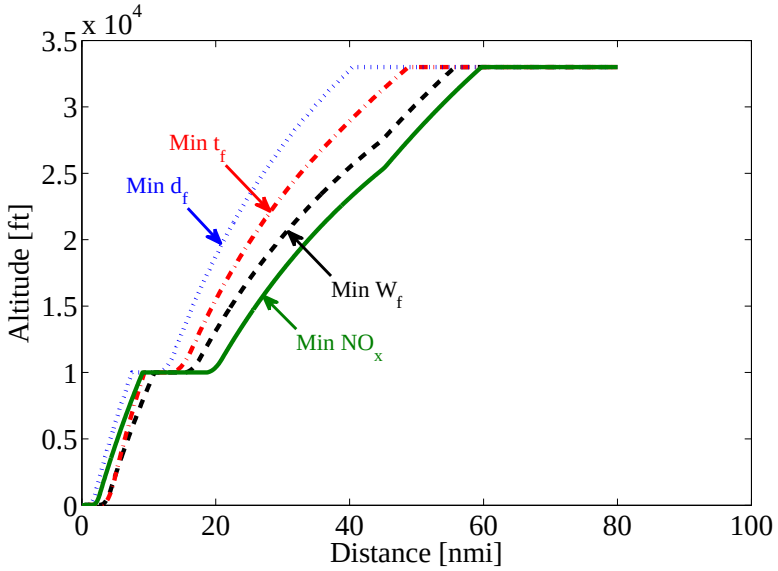

Figure 6.3: Single-criterion optimal climb trajectories.

Table 6.2: Comparison of four single-criterion optimal climb trajectories.

Criterion	Fuel(lbs)	NOx(lbs)	Flight Time(sec)	Distance(nmi)
Min Fuel	1986	49.41	773.4	87.88
Min NO_x	2506	16.54	877.2	84.02
Min Time	1990	60.25	715.1	78.15
Min Distance	1998	60.25	718.9	53.54

indeed close [24]. The minimum-NO_x trajectory is the least steep. As presented in Table 4.1, emissions index of NO_x increases with power setting. Smaller throttle setting is employed during departure and early climb period for the minimum-NO_x trajectory, as shown in Fig. 6.4

Tradeoff relations among the four performance criteria are now studied by first examining two pairwise tradeoffs between fuel burn and climb time, and NO_x emissions and climb time, both with a fixed climb distance. The effect of different climb distances is examined next.

With a specified climb distance, the tradeoffs between fuel burn and climb time are

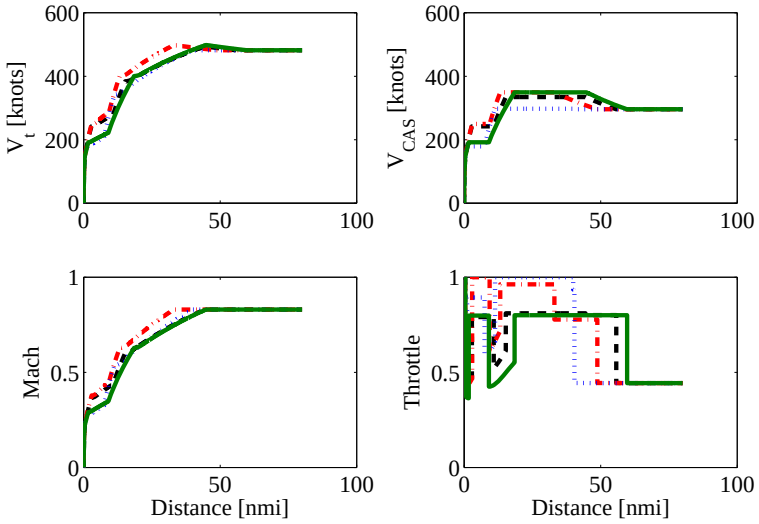

Figure 6.4: Speed and throttle profiles in single-criterion optimal climbs.

studied through the following optimization performance index

$$I = K_f W_{f,c} + K_t t_c \tag{6.21}$$

where the weighting factors K_f, K_t are systematically varied. To reach the fuel-optimal, $K_f = 1$ and $K_t = 0$ are used. And the left end and right end of curve are time-optimal and NO_x-optimal, which were already given in previous results. For the left-half trade-off curve between fuel-optimal and time-optimal, $K_f = 1$ and K_t is selected from 0.1 to 0.8. For right-half trade-off curve between fuel-optimal and NOx-optimal, $K_f = 1$ and K_t is selected from -0.1 to -0.9.

Fig. 6.5 shows that for given climb distance and cruising altitude, there is a best flight time at which the fuel consumption becomes the smallest. As the required climb time deviates (either increases or decreases) from this best climb time, the fuel consumption would increase. The dashed line in Fig. 6.5 represents the corresponding NO_x emissions. It shows that a shorter climb time result in larger NO_x emissions. This is expected because a larger throttle setting is required for a shorter climb time, and emissions index of NO_x increases with throttle setting.

Similarly, the tradeoffs between NO_x emissions and climb time are studied through

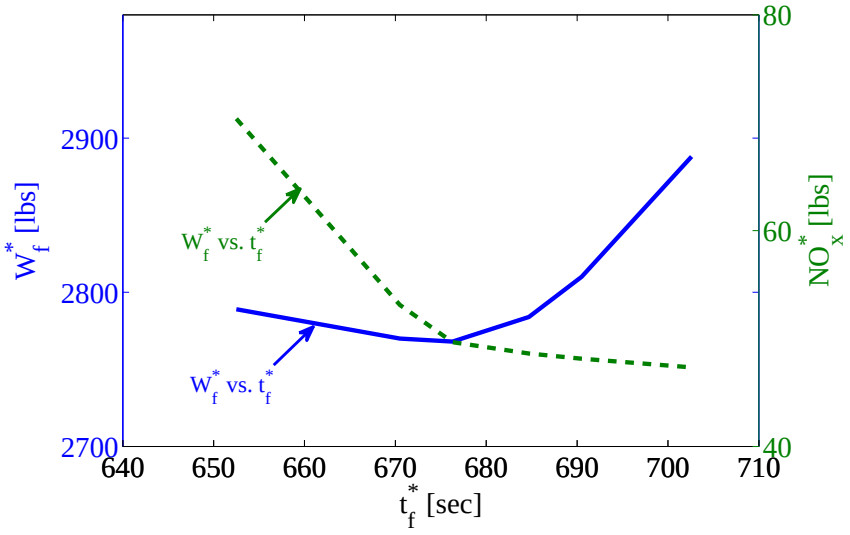

Figure 6.5: Tradeoffs between fuel burn during climb and climb time.

the following optimization performance index with a specified climb distance,

$$I = K_{\mathrm{NO_x}} W_{\mathrm{NO_x},c} + K_c t_c \tag{6.22}$$

Fig. 6.6 indicates that the trends are similar to those in Fig. 6.5, though strictly speaking, the two figures are obtained using different optimization performance indices in Eqs. (6.23) and (6.22). Specifically in Fig. 6.6, the NO_x emissions and climb time are directly optimized. The dashed line shows the resulting fuel consumption. These results indicate that NO_x emissions and climb times represent opposing optimization criteria. To reduce emissions released during climb, the aircraft needs to be flown with small throttle setting, which prolongs the climb time.

Fig. 6.7 shows the effects of the climb distance on the tradeoffs between fuel consumption and climb time. The basic pattern of the tradeoff stays the same, but as the required climb distance increases, the fuel consumption increases. In comparison, Fig. 6.8 shows the effects of the climb distance on the tradeoffs between NO_x emissions and climb time. The basic tradeoff pattern again stays the same. Interestingly, the same level of NO_x emissions may be maintained for different climb distances by adjusting the climb time.

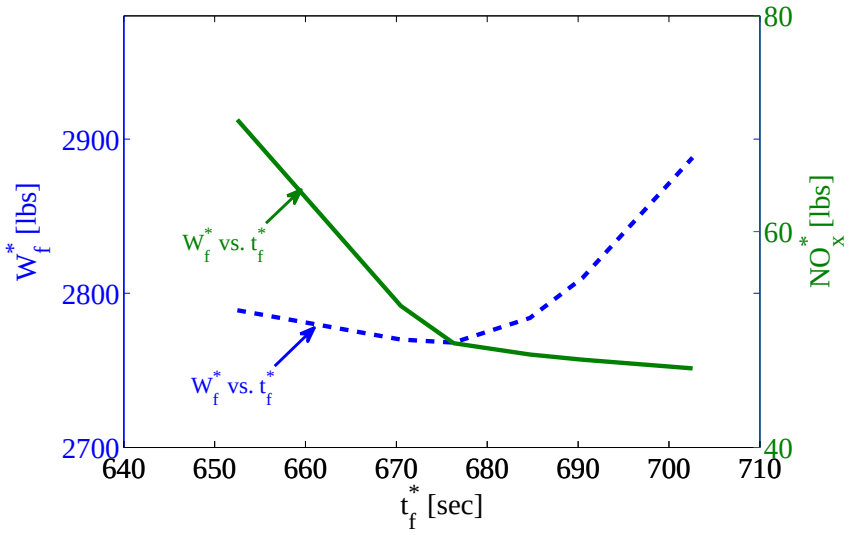

Figure 6.6: Tradeoffs between NO_x emissions during climb and climb time.

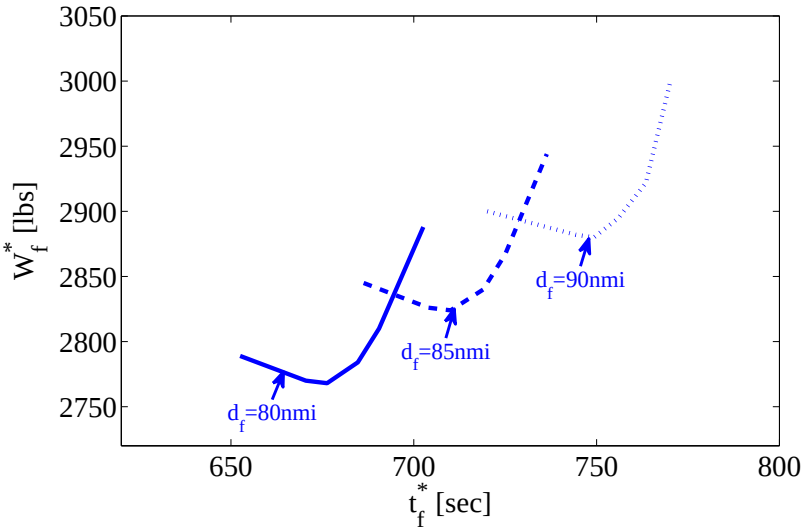

Figure 6.7: Tradeoffs between fuel burn and flight time at different climb distances.

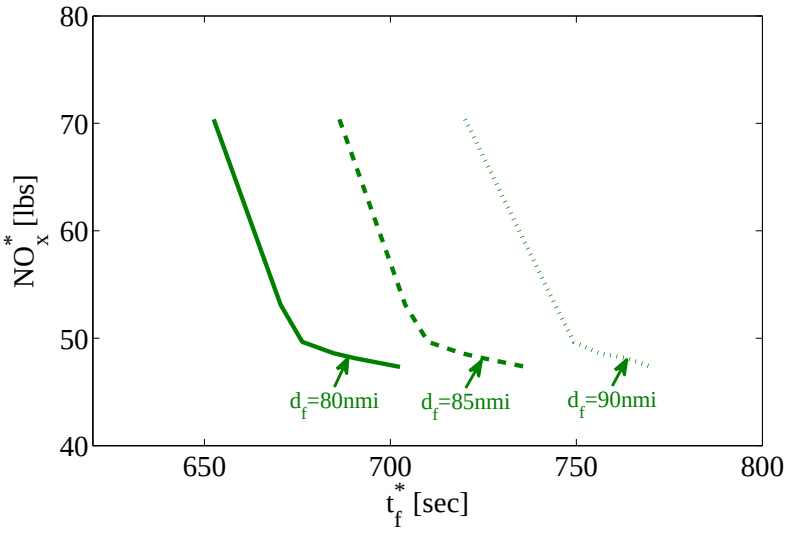

Figure 6.8: Tradeoffs between NO_x and flight time at different climb distances.

Chapter 7

Sensitivity Analysis of Optimized Climb Trajectories

In practical flight operation, it is important to examine the effects of actual flight condition on the quality of generated trajectories. To evaluate the qualities of generated trajectories, closed-loop sensitivities can measure deviations of actual trajectories from generated trajectories caused by modeling errors and/or flight conditions. So closed-loop sensitivity can reflect the predictability of the generated trajectory. Closed-loop sensitivity is no longer the conventional sensitivity concept for trajectory optimization. It is related to the so-called sensitivity function of a feedback system defined by Bode [62], for which Frank [63] gives various methods for calculations or measurements. This paper measure the closed-loop sensitivities to evaluate the differences between actual and generated trajectories when the actual conditions differ from those used in trajectory generation.

After the optimal trajectory is generated, when the aircraft is following the optimal trajectory, because of the existence of uncertainty, the actual trajectory would have deviations from the original one, then the corresponding fuel burn, time cost or emissions would also change. Therefore, closed-loop sensitivity is conduced to study the likely variations of fuel burn, flight time, and emissions in practical operations with existence of uncertainties.

7.1 Different Sensitivity Concepts

Historically, Bode [62] was the first to establish the significance of sensitivity analysis in the design of feedback control systems. He introduced a sensitivity definition in the frequency domain. Beginning around 1958-1960, the number of publications devoted to sensitivity analysis in the time domain increased considerably thanks to the development of state space methods in control engineering and the availability of digital computer. In 1963 Dorato [64] called attention to the problem of parameter sensitivity of performance index of optimal control systems. Thereafter, many papers were published sharpening this definition of sensitivity [65, 66, 67, 68, 69, 70] gives detailed analytical treatments of parametric sensitivities.

The open-loop sensitivity of a trajectory attribute I (e.g. fuel consumption or emissions) with respect to a certain model parameter may be calculated by repeating the trajectory generation process with different values of the model parameter. For example, a generic model parameter can be expressed as

$$w = w^n + dw \tag{7.1}$$

in which w^n is its nominal value. Using a forward difference scheme, the open-loop sensitivity of I with respect to the generic parameter can be expressed as

$$(\frac{\partial I}{\partial w})_{OL} \approx \frac{I^*(w^n + dw) - I^*(w^n)}{dw} \tag{7.2}$$

where $I*()$ represent the value of the optimization performance index obtained from trajectory optimization.

Table. 7.1 present the open-loop sensitivities for the climb phase due to constant modeling errors in horizontal wind, vertical wind, and temperature. Due to the complex segmented structures, these sensitivities are computed numerically with a forward difference scheme, where each value of the attribute is obtained by solving the optimal trajectory generation problem with a different model parameter. These sensitivities indicate that vertical wind errors would affect estimated fuel and time more than horizontal wind errors during the climb phase. Temperature affects the most among the three.

Table 7.1: Open-loop sensitivities for minimum-fuel climb trajectories.

Model Parameters	δW_{fc}lbs	δt_csec	δs_cnmi
$\delta W_x + 5$ft/s	0	0	0.41
$\delta W_h - 5$ft/s	77	6.0	1.0

In essence, open-loop sensitivities measure variations of generated trajectories when model parameters change. They reveal the inherent variability of the trajectory generation process. Overly large open-loop sensitivities point to the need to improve modeling accuracies, knowledge of initial conditions, and/or solution algorithms. However, they do not directly reflect the ability of an aircraft to follow a trajectory in actual flights.

In actual flights, selected features of generated trajectories (e.g. Mach number, altitude) are used as commands for the pilot or autopilot to track. Because the actual flight environment is different from models used in trajectory generations, actual trajectories differ from generated trajectories. These differences reflect trajectory predictability.

In this context, closed-loop sensitivities measure deviations of actual trajectories from generated trajectories when flight conditions differ from their models in the trajectory generation process, where the actual trajectories are obtained through closed-loop tracking of certain features of the generated trajectories in the presence of uncertainties. Mathematically, closed-loop sensitivities can be expressed as

$$(\frac{\partial I}{\partial w})_{CL} \approx \frac{I^{CL}(w^n + dw) - I^*(w^n)}{dw} \tag{7.3}$$

where $I^{CL}(w^n + dw)$ is the value of the optimization performance index obtained when closed-loop trajectory tracking is used.

Closed-loop sensitivity is no longer the conventional sensitivity concept for trajectory optimization. It is related to the sensitivity function of a feedback system defined by Bode [62], for which Frank [63] gives various methods for calculations or measurements. Youla and Dorato [69] compares sensitivities of open and closed-loop dynamic systems. Closed-loop sensitivities are used in Ref. [71] to evaluate descent trajectories.

Closed-loop sensitivities depend on trajectory tracking laws. For the same nominal trajectory but different trajectory tracking laws, closed-loop sensitivities can be different.

7.2 Closed-Loop Sensitivities with Respect to Vertical Wind Uncertainties

During the climb and descent phase, a major source of uncertainty for trajectory tracking lies in the vertical wind speed. As an example of the closed-loop sensitivity analysis, uncertainties in the vertical wind speed are used to examine their effects on the likely variations of fuel burn, NO_x emissions, and climb time.

Fig. 7.1 shows the likely variations of actual trajectories when either the minimum-fuel, the minimum-time, or the minimum-NO_x climb trajectory is tracked. Two levels of vertical wind variations are considered: $W_h = 2$, 5ft/s, in addition to its nominal value of $W_h = 0$. Results qualitatively indicate that when the minimum-NO_x trajectory is tracked, the actual trajectories may vary the most.

This is confirmed by the calculated closed-loop sensitivities. For each optimal trajectory, the closed-loop sensitivities are calculated for the variations of fuel burn, NO_x emissions, climb time with respect to the vertical wind speed, and are summarized in Table. 6. With a larger vertical wind, the aircraft can reach the cruising altitude earlier, thus resulting in less fuel and time. As a result, the closed-loop sensitivities all have negative signs.

Table 7.2: Closed-loop Sensitivities with respect to wind for in optimized climb.

Optimization Criterion	$\frac{\partial W_f}{\partial W_h}[\frac{lbs}{ft/s}]$	$\frac{\partial t_f}{\partial W_h}[\frac{s}{ft/s}]$	$\frac{\partial \mathrm{NO_x}}{\partial W_h}[\frac{lbs}{ft/s}]$
minW_f	-13.45	-0.30	-0.38
mint_f	-10.90	-0.24	-0.53
min$\mathrm{NO_x}$	-15.25	-0.49	-0.43

Table 7.2 indicates that the sensitivities of the minimum-fuel and minimum-time trajectories are close, as expected. On the other hand, the minimum-NO_x trajectory shows more likely variations of fuel burn and climb time in the presence of vertical wind uncertainties, though its likely variations of NO_x emissions are much smaller. In other words, when the minimum-NO_x trajectory is tracked in actual flights, the actual NO_x emissions will be close to the predicted value, but actual fuel burns and climb times will differ significantly from their predicted values.

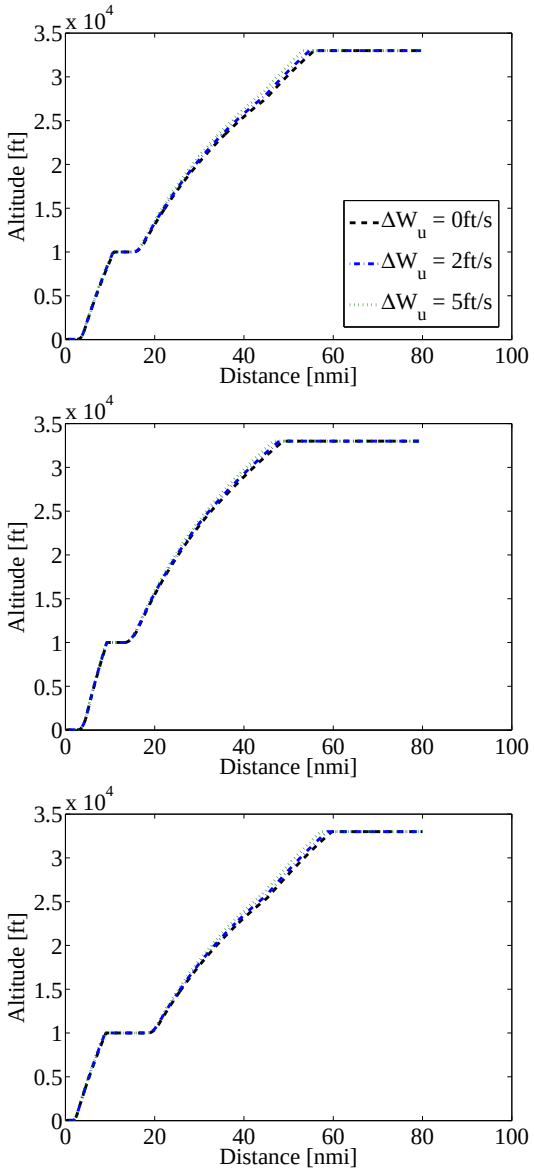

Figure 7.1: Climb trajectory variations due to vertical wind uncertainty: (a) min-fuel trajectory, (b) min-time trajectory, and (c) min-NO_x trajectory.

Chapter 8

Optimal Descent Flights and Their Sensitivities

While descent flights produce smaller emissions and fuel burns than climbs, it is still useful to calculate optimal descent trajectories and compare their performances with those of optimal climbs. These results can provide useful references to airport scheduling to minimize environmental impacts, which need to consider both departures and arrivals.

8.1 Formulation of Optimal Descent Trajectory Planning

Fig. 8.1 below shows a representative descent profile that consists of a series of flight segments from top of descent (TOD) to touchdown. Table. 8.1 defines these segments in the climb profile and the corresponding capture conditions.

Table 8.1: Segments and capture conditions for a representative descent profile.

No.	Segment Type	Flight Objectives	Capture Condition
D0	Level Cruise	M_{cr}, $h_{p,cr}$	Reaching time or dist
D1	Descent with Constant Mach	M_c, κ_c	Reaching a CAS
D2	Descent with Constant CAS	$V_{CAS,c}$, κ_c	Reaching an altitude
D3	Level deceleration	$\dot{V}_{t,c}$, $h_{p,c}$	Reaching a CAS
D4	Descent with constant CAS	$V_{CAS,c}$, κ_c	Reaching an altitude
D5	Descent with deceleration	$\dot{V}_{t,c}$, $\dot{h}_{p,c}$	Reaching a CAS, runway

Denoting descent flight objectives of different segments in the flight profile as p_{dk}

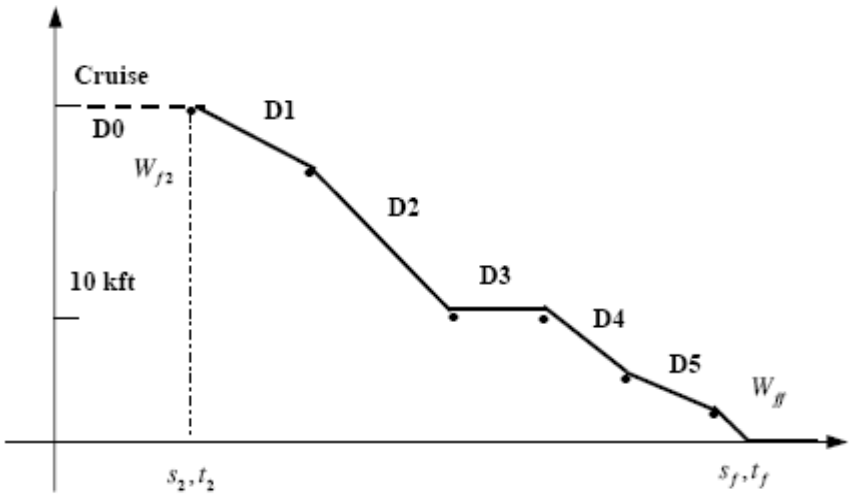

Figure 8.1: A representative descent trajectory

, $k = 1, 2, ..., N_d$, where N_d is the total number of objectives in each segment during descent, and

$$p_{dk,min} \leq p_{dk} \leq p_{dk,max} \tag{8.1}$$

where constraints on each flight objective come from the motion constraints discussed above, the descent phase decision parameter vector can then be expressed as

$$\vec{p}_d = [p_{d1}, p_{d2}, ..., p_{dN}] \tag{8.2}$$

An optimal descent flight can be formulated to minimize the performance index

$$\min_{\vec{p}_d} I(\vec{p}_d) = K_f W_{f,d} + K_t t_{f,d} + K_{\mathrm{NO_x}} W_{\mathrm{NO_x},d} + K_s S_d \tag{8.3}$$

subject to Eqs. (2.1)-(2.5), and appropriate initial conditions at the top of descent

$$M_{t_0} = M_{cr}, \gamma_{t_0} = 0, h_{t_0} = h_{cr}, s_{t_0} = 0, m_{t_0} = m_{cr} \tag{8.4}$$

parameters bounded in Eq. (6.8), and the final touchdown condition

$$V(t_d) = V_f, h(t_d) = h_f \tag{8.5}$$

Sometimes, the total climb distance is specified: $s(t_d) = s_d$. In this paper, it is assumed that $h = 50$ft and $V_f = 200$ft/sec, and when applicable $s_d = 80$nmi.

In Eq. (6.10), the fuel consumption during descent is calculated as

$$W_{f,d} = [m(t_0) - m(t_d)]g \tag{8.6}$$

and the NOx emissions below 3000ft are calculated from

$$W_{\mathrm{NO_x},d} = \int_{t_2}^{t_d} \mathrm{EI}_{\mathrm{NO_x}} \cdot \dot{W}_f dt \tag{8.7}$$

where $h(t_2) = 3000$ft, and $\dot{W}_f = c_{tsfc}T$.

8.2 Calculated Optimal Descent Trajectories

Fig. 8.2 and 8.3 present optimal descent trajectories obtained with each of the four optimization criteria: fuel burn, NO_x emissions, descent time, and descent distance. Fuel burn, descent time, and descent distance are all calculated from the top of descent (TOP) to runway touchdown. In comparison, NO_x emissions are calculated below 3,000 ft.

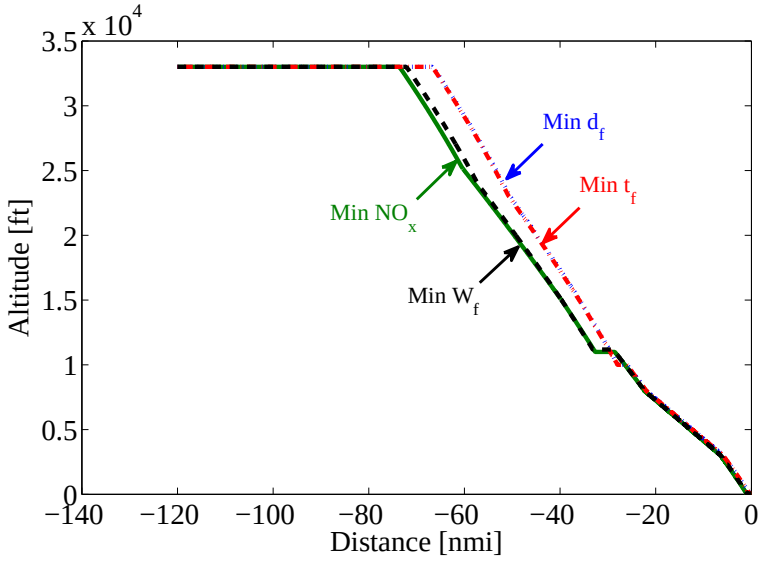

Figure 8.2: Single-criterion optimal descent trajectories.

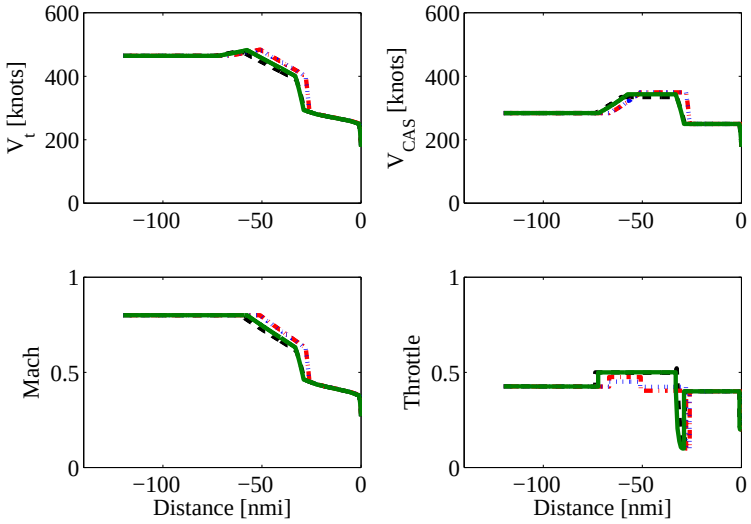

Figure 8.3: Speed and throttle profiles of single-criterion optimal descent trajectories.

For the throttle setting and aircraft flight angle has lower limit during descent, optimal descent trajectories under different performance indices did not produce too much difference. The minimum-fuel descent requires a somewhat longer horizontal distance during the descent in order to employ idle(smaller or nearly idle) thrust all the way. In comparison, the minimum-time and minimum-distance descent trajectories are closed. They employ relatively larger speed profiles all the way to 10,000 ft, where it reduces the speed drastically in order to satisfy the ATC speed constraint. As a result, the minimum-time/distance descent employs a level-off segment to slow down. Smaller thrust needs to be employed to reduce NO_x as much as possible, but the minimum-fuel descent trajectory already reached the lower limit of thrust all the way. So the minimum-NO_x descent trajectory is not notably different from minimum-fuel trajectory.

Tab. 8.2 shows the corresponding performance measures of the four single-criterion optimal descent trajectories. Clearly, lower NOx emissions below 3,000 ft can be achieved at the expense of more fuel burns, longer descent time, and longer distance traveled.

Fig. 8.4 shows the tradeoffs among fuel burns, NO_x emissions, and descent times for a fixed descent distance. These patters are similar to those in optimal climbs. In

Table 8.2: Comparison of four single-criterion optimal descent trajectories.

Criterion	Fuel(lbs)	NOx(lbs)	Flight Time(sec)	Distance(nmi)
Min Fuel	426.4	4.87	1563.1	99.06
Min NO_x	857.9	3.80	2324.7	147.6
Min Time	560.1	5.37	1537.5	106
Min Distance	446.5	5.78	1527.9	89.25

particular, there is a best descent time at which the fuel consumption is the lowest. Deviations of descent time from this optimal value will require more fuel burns. This means that both time advance and delay causes additional fuel burns, even though time advances to a certain extend do not cause as significant fuel burns as delays. Lower NO_x emissions below 3,000 ft are achieved at the expense of longer descent times and in most cases, more fuel burns.

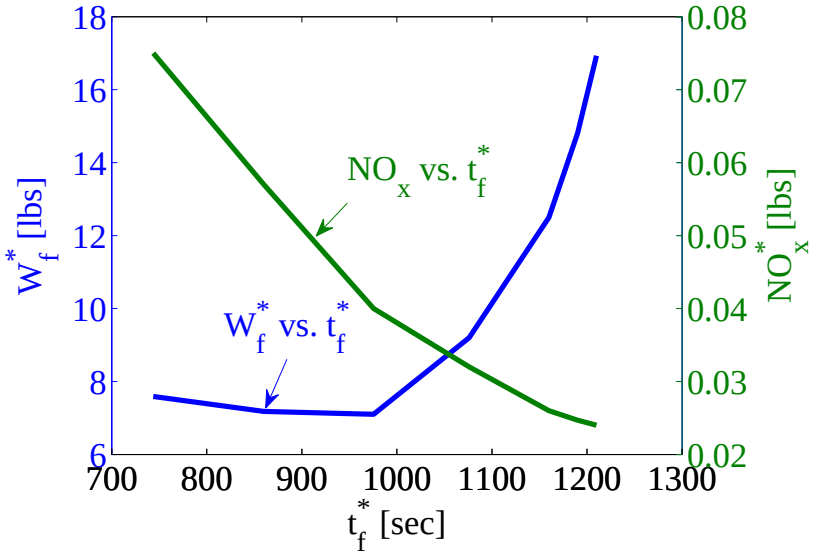

Figure 8.4: Tradeoffs between fuel burn, NOx and flight time during descent.

8.3 Closed-Loop Sensitivities of Optimal Descent Trajectories

Likely variations of actual descent trajectories when a single-criterion optimal descent trajectory is followed in the presence of vertical wind uncertainties are also studied, as shown in Fig. 8.5. The corresponding closed-loop sensitivities are presented in Table 8.3. A positive vertical wind would prolong the descent process, so the total descent distance from TOD to landing is larger, and all the numbers in Table 8.3 are positive. These results show that the minimum-NO_x descent trajectory is the most sensitive to vertical wind uncertainties in all performance criteria of interest.

Table 8.3: Closed-loop Sensitivities with respect to wind for in optimized descent.

Optimization Criterion	$\frac{\partial W_f}{\partial W_h}[\frac{lbs}{ft/s}]$	$\frac{\partial t_f}{\partial W_h}[\frac{s}{ft/s}]$	$\frac{\partial \mathrm{NO_x}}{\partial W_h}[\frac{lbs}{ft/s}]$
minW_f	85.75	92.85	1.08
mint_f	78.45	80.80	1.00
min$\mathrm{NO_x}$	88.30	85.70	1.10

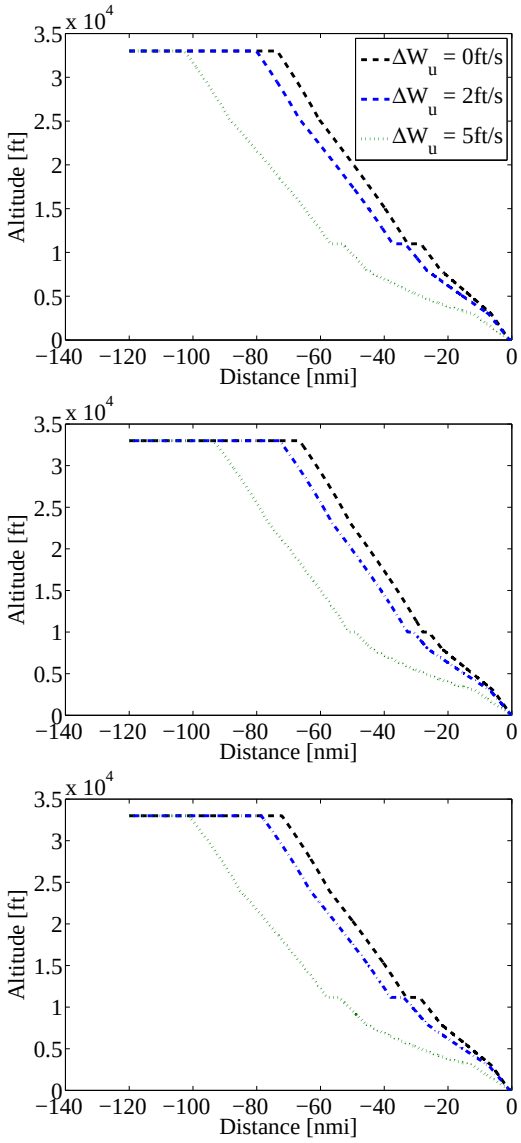

Figure 8.5: Descent trajectory variations due to vertical wind uncertainty: (a) min-fuel trajectory, (b) min-time trajectory, and (c) min-NO_x trajectory.

Chapter 9

Optimal Complete Trajectory Planning

In previous sections, climb and descent phases were first analyzed separately. We now consider complete trajectories from liftoff to touchdown consisting of all three phases of climb, cruise, and descent, shown in Fig. 5.1. Strictly speaking, an optimal climb does not necessarily lead to an optimal complete trajectory. On the other hand, departure and arrival flights are handled by separate ATC facilities. It is therefore desirable to understand choices of optimal flights for each phase.

In general, there can be different cruise strategies. The three common ones either practiced or discussed in the literature employ constant altitude/constant speed, cruise climb, and stepped-climb. In this paper, it is assumed that the cruise phase consists of level flight at a constant pressure altitude and constant speed, which can be equivalently expressed in terms of either true airspeed or Mach number. As a result, there are two objective commands for the cruise phase: pressure altitude and true airspeed.

Because the origin and destination are specified for a complete flight, there are in general two fundamental considerations in optimizing complete trajectories: flight time and fuel consumption. A linear combination of the two is often called the cost index. In optimal trajectory generations, objectives of all flight segments in a complete trajectory can be selected to minimize the total flight time, the total fuel consumption, or their appropriate combinations.

Fig. 9.1 and 9.2 shows the optimal complete trajectories obtained with the two performance indices and the assumption of perfect tracking. Minimum-time and minimum fuel complete trajectories differ in an expected way. The minimum-time trajectory utilizes a higher speed and a lower cruising altitude, whereas the minimum-fuel trajectory employs a lower speed and climbs to a higher cruise altitude for better efficiency. In the climb phase, the minimum-fuel trajectory has a steeper climb than the minimum-time trajectory. In the descent phase, the minimum-fuel trajectory employs idle thrust all the way, as expected, whereas the minimum-time trajectory employs overall higher speed. Improvement from the initial trajectory guess again suggests that a well-designed solution algorithm can provide noticeable benefits.

Fig. 9.3 illustrates a unique feature of the tradeoff between optimal flight time and optimal fuel consumption in complete trajectories. For a given origin-destination pair, there is a best flight time at which the fuel consumption achieves the absolute minimum for the trip. If the required flight time is smaller than this best flight time, the required fuel consumption would increase. Interestingly if the required flight time is longer than the best flight time, the fuel consumption would also increases. Therefore, aircraft arrivals should be scheduled around the best flight times under given conditions. Either time advance or delay will require additional fuel consumptions.

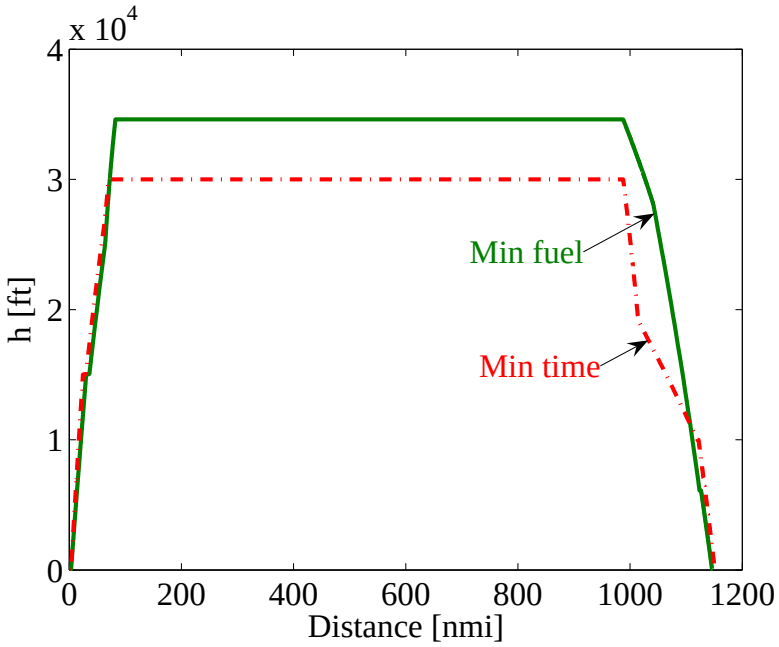

Figure 9.1: Altitude histories of optimal complete trajectories.

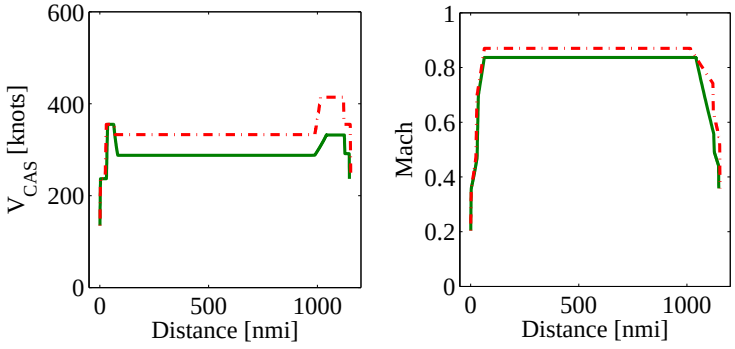

Figure 9.2: Speed histories of optimal complete trajectories.

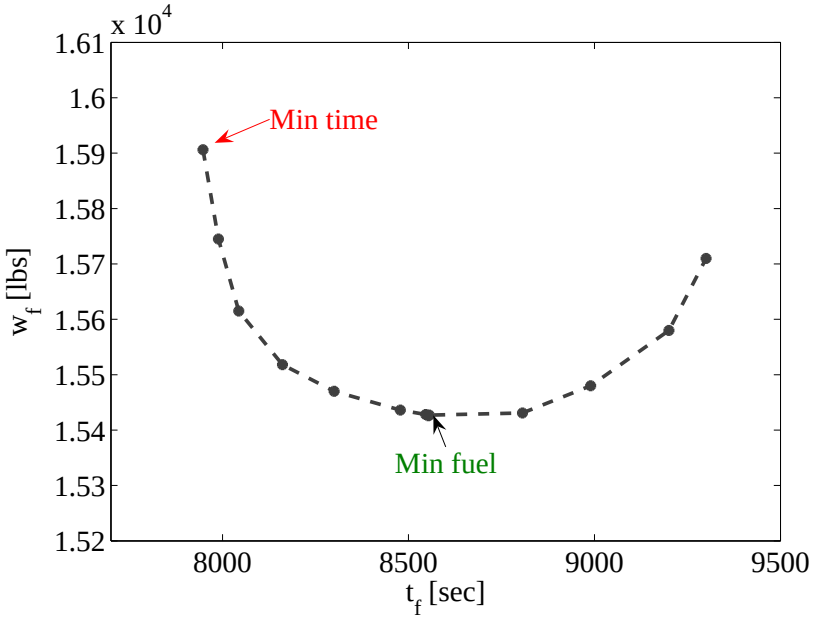

Figure 9.3: Tradeoff between flight time and fuel in complete trajectories.

Chapter 10

Conclusion and Discussion

The air traffic has been growing steadily over the last two decades and is projected to grow further. The growth has caused significant congestions, cost increases, and environmental issues. It has become highly desirable to develop computer automation tools to assist air traffic controllers for the safe and efficient handling of air traffic. Optimal flight trajectory generation is core to all computer-based automated air traffic systems. The goal of this thesis is to lay a theoretical foundation in terms of problem formulations and numerical solutions for the optimal trajectory generation.

This thesis examined different choices of optimization performance indices in trajectory generations for individual aircraft trajectory planning and prediction in ATC system, and examined sensitivity concepts to evaluate generated trajectories. Trajectory generation process is formulated as a parameter optimal control problem that minimizes flight time, fuel consumption, flight emissions, or when applicable, flight distance traveled respectively for the climb phase, the descent phase or the entire trajectory. A gradient algorithm is developed to obtain accurate numerical solutions for these trajectory generation problems and can also be used to assess other solution algorithms.

First, the thesis studies characteristics of climb and descent trajectories separately in the ATC system that minimize fuel burn, NO_x emissions, flight time, and flight distance respectively. Basic patterns of tradeoffs among these performance criteria are also examined. The production of CO_2 is directly proportional to fuel burn, so minimizing CO2 is equivalent to minimizing fuel burn. In addition, closed-loop sensitivities are calculated to assess likely variations of optimized trajectories in practical operations in

the presence of uncertainties.

In this thesis, two-dimensional point-mass equations of motion in the vertical plane are used to model aircraft flight, with available aircraft performance models of a generic commercial aircraft. Commercial flight profiles in ATC are modeled as a series of flight segments, where each segment is specified through two flight objectives. Standard atmosphere conditions are assumed with zero nominal winds. In computing aircraft emissions, a fuel flow-related model for computing NO_x emissions is adopted. Climb and descent flights in ATC are formulated as parameter optimal control problems, subject to aircraft equations of motion, typical motion constraints, and appropriate boundary conditions. A gradient algorithm is developed for numerical solutions. Closed-loop sensitivities are computed with respect to vertical wind uncertainties.

For climb flights, the minimum-distance climb trajectory produces the steepest path. The minimum-time and minimum-fuel trajectories are steeper than the minimum-distance climb. In comparison, the minimum-NO_x trajectory uses a smaller throttle setting in order to reduce emissions below 3,000 ft, and takes a longer time, more fuel, as well as a longer distance to reach cruise conditions. For descent flights, because the throttle setting and aircraft flight angle has lower limit during descent, optimal descent trajectories under different performance indices did not produce too much difference. In particular, the minimum-fuel descent requires a somewhat longer horizontal distance during the descent in order to employ nearly idle or lower limit thrust all the way. The minimum-time and minimum-distance descent trajectories are close. Smaller thrust needs to be employed to reduce NO_x as much as possible, but the minimum-fuel descent trajectory already reached the lower limit of thrust all the way. So the minimum-NO_x descent trajectory is not notably different from minimum-fuel trajectory.

In both climb and descent, the basic tradeoff patterns among fuel burn, flight time, and NO_x emissions are similar. In both cases, NO_x emissions at low altitudes may be reduced at the expense of prolonged flights and additional fuel burns. For same specified flight distance and cruise conditions, there is a best flight time at which the fuel consumption is the smallest. As the flight time deviates from this best time (due to either time advance or delay), the fuel consumption increases.

Next, two concepts of sensitivities are examined. Open-loop sensitivities measure the variations of generated trajectories due to changes of model parameters, and they

reflect the reliability of the trajectory generation process. In comparison, closed-loop sensitivities measure deviations of actually flown trajectories from generated trajectories when actual conditions differ from their modeled values. They reflect trajectory predictability. In the thesis, closed-loop sensitivities are computed with respect to uncertainties of vertical wind speed. Generally, a positive variation of vertical wind speed will expedite climb process but prolong descent process. Thus, vertical wind speed can save climb fuel, time, distance as well as emissions for climb flights, but it will increase or prolong these performances for descent flight.

For complete trajectory planning from liftoff to touchdown consisting of all three phases of climb, cruise, and descent, total flight fuel and flight time are optimized separately and then evaluated with respect to their trade-off. The results shows that, for a given origin-destination pair, there is a best flight time at which the fuel consumption achieves the absolute minimum for the trip. Therefore, to save the complete fuel consumption, aircraft arrivals should be scheduled around the best flight times under given conditions. Either time advance or delay will require additional fuel consumptions.

References

[1] Joint Planning and Development Office. Next generation air transportation system: Integrated plan. Technical report, 2004.

[2] D. Wu, Y. J. Zhao, and B. Capozzi. A systematic analysis of surface trajectory models. *Air Traffic Control Quaterly*, 19(2):115–145, 2011.

[3] *Intergovernmental Panel on Climate, Aviation and the Global Atmosphere*, pages 124–127. Cambridge University Press, Cambridge, England, UK, 1999.

[4] F. Collier. Overview of nasa's environmentally responsible aviation (era) project. Technical report, January 2010. 48th AIAA Aerospace Sciences Meeting.

[5] International Civil Aviation Organization. *ICAO Annex 16 Volume II: Aircraft Engine Emissions*, 2nd edition, 1993.

[6] International Civil Aviation Organization. *Airport Air Quality Guidance Manual*, 2007. Doc.9889.

[7] Air quality procedures for civilian airports and air force bases. Technical report, April 1997. Rept. FAA-AEE-97-03 AL/EQ-TR-1996-0017.

[8] J. E. Penner. *Aviation and the Global Atmosphere*, pages 185–217. Cambridge University Press, 1999.

[9] J. B. Heywood. *Internal Combustion Engine Fundamentals*, pages 567–667. McGraw-Hill, 1988.

[10] N. R. Zagalsky, R. E. Irons, and R. L. Schultz. The energy state approximation and minimum-fuel fixed-range trajectories. *Journal of Aircraft*, 8(8), 1971.

[11] R. L. Schultz and N. R. Zagalsky. Aircraft performance optimization. *Journal of Aircraft*, 9(2):108–114, February 1971.

[12] J. F. Barman and H. Erzberger. Fixed-range optimal trajectories for short haul aircraft. *Journal of Aircraft*, 13(10):748–754, 1976.

[13] A. J. Calise. Extended energy management methods for flight performance optimization. *AIAA Journal*, 15(3):314–321, 1976.

[14] H. Erzberger and H. Lee. Constrained optimum trajectories with specified range. *Journal of Guidance, Control, and Dynamics*, 3(1):78–85, 1980.

[15] J. W. Burroughs. Fuel-optimal aircraft trajectories with fixed arrival times. *Journal of Guidance and Control*, 6(1):14–19, January-February 1983.

[16] A. J. Calise. Singular perturbation techniques for on-line optimal flight-path control. *Journal of Guidance and Control*, 3(4):398–405, 1981.

[17] D. P. Price, J. C. Calise, and D. D. Moerder. Piloted simulation of an onboard trajectory optimization algorithm. *Journal of Guidance and Control*, 7(3):355–360, 1984.

[18] A. Chakravarty. Four-dimensional fuel-optimal guidance in the presence of winds. *Journal of Guidance, Control, and Dynamics*, 8(1):16–22, January-February 1985.

[19] R. L. Schultz. Three-dimensional trajectory optimization for aircraft. *Journal of Guidance, Control, and Dynamics*, 13(6):936–943, November-December 1990.

[20] J. A. Sorenson and M. H. Waters. Generation of optimum vertical profiles for an advanced flight management system. Technical report, March.

[21] G. Menga and H. Erzberger. Time-controlled descent guidance in uncertain winds. *Journal of Aircraft*, 1(2), March-April 1978.

[22] H. Erzberger. Automation of on-board flightpath management. Technical report, December.

[23] R. A. Slattery and Y. J. Zhao. Trajectory synthesis for air traffic automation. *Journal of Guidance, Control, and Dynamics*, 20(2):232–238, March-April 1997.

[24] F. J. Hale. *Introduction to Aircraft Performance, Selection, and Design*, chapter 10. John Wiley & Sons, 1984. Sections 4-2 to 4-5.

[25] N. X. Vinh. *Flight Mechanics of High-Performance Aircraft*, chapter 2. Cambridge University Press, 1993. Section 4.4, Appendix 2.

[26] D. G. Hull. *Fundamentals of Airplane Flight Mechanics*. Springer, 2007.

[27] J. D. Anderson. *Aircraft Performance and Design*, chapter 3 & 5. Springer, 1999.

[28] C. Gong. Kinematic airport surface trajectory model development. Hilton Head, South Carolina, September 2009. AIAA Aviation Technology, Integration, and Operations Conference (ATIO). AIAA-2009-7076.

[29] B. Capozzi, S. Pledgie, M. Kistler, B. Wood, and J. Rebollo. Surface trajectory characterization report. Technical report, NASA NRA, Mosaic ATM, and University of Minnesota, April 2010. NRA Contract NNA09DA89C2010.

[30] V. H. L. Cheng and G. D. Sweriduk. Trajectory design for aircraft taxi automation to benefit trajectory-based operations. In *Proceedings of the 7th Asian Control Conference*, Hong Kong, China, August 2009.

[31] T. Rentas, S. M. Green, and K. T. Cate. haracterization method for determination of trajectory prediction requirements. Hilton Head, South Carolina, 2009. AIAA, 9th AIAA Aviation Technology, Integration, and Operations Conference (ATIO).

[32] C.E. Seah and I. Hwang. Terminal-area aircraft tracking using hybrid estimation. *Journal of Guidance, Control, and Dynamics*, 32(3), May-June 2009.

[33] S. Pledgie, S. Atkins, and C. Brinton. Methods for aircraft state estimation from airport surface surveillance. Chicago, Illinois, August 2009. 2009 AIAA Guidance, Navigation, and Control Conference.

[34] K. Lindsay, S. Green, S. Mondoloni, and M. Paglione. Common trajectory modeling for national airspace system decision support tools. Technical report, The MITRE Corporation, Mclean, Virginia, June 2002. MP 02W0000115.

[35] R. Paielli. Trajectory specification for high-capacity air traffic control. *AIAA Journal of Aerospace Computing, Information, and Communication*, 2(9), 2005.

[36] R. A. Vivona, K. T. Cate, and S. M. Green. Abstraction techniques for capturing and comparing trajectory predictor capabilities and requirements. Honolulu, Hawaii, August 2008. AIAA Guidance, Navigation, and Control (GNC) Conference and Exhibit.

[37] M. Paglione, C. Garcia-Avello, S. Swierstra, R. Vivona, and S. Green. A collaborative approach to trajectory modeling validation. Washington, DC, October 2005. 24th Digital Avionics Systems Conference.

[38] J. P. Clarke. *A System Analysis Methodology for Developing Single Events Noise Abatement Procedures*. Ph.d. thesis, Massachusetts Institute of Technology, Cambridge, Massachusetts, January 1997.

[39] L. J. J. Erkelens. Development of noise abatement procedures in the netherlands. Technical report, National Aerospace Lab, November 1999. NLR TR 999386.

[40] H. G. Visser and R. A. A. Wijnen. Optimization of noise abatement departure trajectories. *Journal of Aircraft*, 38(4), July-August 2001.

[41] R. A. A. Wijnen and H. G. Visser. Optimal departure trajectories with respect to sleep disturbance. *Aerospace Science and Technology*, 7:81–91, 2003.

[42] N. T. Ho and J. P. Clarke. Methodology for optimizing parameters of noise-abatement approach procedures. *Journal of Aircraft*, 44(4), July-August 2007.

[43] R. Torres, J. Chaptal, C. Bes, and J. B. Hiriart-Urruty. Optimal, environmentally friendly departure procedures for civil aircraft. *Journal of Aircraft*, 48(1), January-February 2011.

[44] E. Torenbeek. Cruise performance and range prediction reconsidered. *Progress in Aerospace Sciences*, 33:285–321, 1997.

[45] J. D. Mattingly, W. H. Heiser, and D. T. Pratt. *Aircraft Engine Design*, pages 38,71. AIAA Education Series, 2nd edition, 2002.

[46] S. Lukachko and I. Waitz. Effects of engine aging on aircraft nox emissions. In *ASME International Gas Turbine and Aeroengine Congress and Exhibition*, June 1997. ASME Paper 97-GT-386.

[47] D. DuBois and G. C. Paynter. Fuel flow method 2 for estimating aircraft emissions. *Society of Automotive Engineers*, August 2002. No. TP 2006-1-1987.

[48] United Kingdom Civil Aviation Authority. Icao engine emissions databank. http://www.caa.co.uk, April 2008.

[49] Y. Zhao and R. A. Slattery. Capture conditions for merging trajectory segments to model realistic aircraft descents. *Journal of Guidance, Control, and Dynamics*, 19(2):453–460, March-April 1996.

[50] D. McRuer. Human dynamics in man-machine systems. *Automatica*, 16(3):237–253, May 1980.

[51] R. A. Hess. *Feedback Control Models Manual Control and Tracking, Handbook of Human Factors and Ergonomics*, chapter 33, pages 1276–1294. John Wiley & Sons, Inc., 2nd edition, 1997.

[52] Parag H. B., Dean A. P., and Charles E. T. Predicting lane position for roadway departure prevention. In *Proceedings of the IEEE Intelligent Vehicles Symposium*, 1998.

[53] R. Horowitz and P. Varaiya. Control design of an automated highway system. In *Proceedings of the IEEE*, 2000.

[54] C. G. Atkeson, A. W. Moore, and S. Schaal. Locally weighted learning. In *Artificial Intelligence Review*, 1997.

[55] K. A. Gluck and R. W. Pew. *Modeling Human Behavior with Integrated Cognitive Architectures.* Lawrence Erlbaum Associates, Mahwah, New Jersey, 2005.

[56] D. C. Foyle and B. L. Hooey. *Human Performance Modeling in Aviation*, chapter 1, 2 & 4. CRC Press, Boca Raton, Florida, 2008.

[57] J. Betts. Survey of numerical methods for trajectory optimization. *Journal of Guidance, Control, and Dynamics*, 21(2):193–207, 1998.

[58] C. R. Hargraves and S. W. Paris. Direct trajectory optimization using nonlinear programming and collocation. *Journal of Guidance, Control, and Dynamics*, 10(4):338–342, July-August 1987.

[59] A. L. Herman and B. A. Conway. Direct optimization using collocation based on high-order gauss-lobatto quadrature rules. *Journal of Guidance, Control, and Dynamics*, 19(3):592–599, May-June 1996.

[60] D. G. Hull. Conversion of optimal control problems into parameter optimization problems. *Journal of Guidance, Control, and Dynamics*, 20(1):57–60, 1997.

[61] F. Fahroo and I. M. Ross. Direct trajectory optimization by a chebyshev pseudospectral method. *Journal of Guidance, Control, and Dynamics*, January-February 2002.

[62] H. W. Bode. *Network Analysis and Feedback Amplifier Design.* Van Nostrand Reighold, Princeton, New Jersey, 1945.

[63] P. M. Frank. *Introduction to System Sensitivity Theory*, chapter 4-5. 1978.

[64] P. Dorato. On sensitivity in optimal control system. *IEEE Trans, Autom.*, pages 256–257, 1963. Contr. 8.

[65] B. Pagurek. Sensitivity of the performance of optimal linear control systems to parameter variations (short paper). *IEEE Trans, Autom.*, pages 178–180, 1965. Contr. 10.

[66] R. A. Rohrer and M. Sobral. Sensitivity considerations in optimal system design. *IEEE Trans, Autom.*, pages 43–48, 1965.

[67] M. Sobral. Sensitivity in optimal control systems. *IEEE Proceedings*, 56:1644–1652, 1968.

[68] H. S. Witsenhausen. On the sensitivity of optimal control system. *IEEE Trans. Autom.*, 1965. Contr. 10.

[69] D. C. Youla and P. Dorato. On the comparison of the sensitivity of open-loop and closed-loop optimal control systems. *IEEE Trans. Autom.*, pages 186–188, 1968. Contr. 13.

[70] W. P. Hallman. Sensitivity analysis for trajectory optimization problems. page 14, Reno, Nevada, January 1990. AIAA, Aerospace Science Meeting, 28th.

[71] M. R. Jackson and Y. J. Zhao. Sensitivities of trajectory prediction in air traffic management. *Journal of Guidance, Control, and Dynamics*, 22(2):219–228, March-April 1998.

Appendix A

Glossary and Acronyms

A.1 Glossary

a	Speed of sound
A	Nose wheel of aircraft
B, C	Rear wheels of aircraft
$c.g.$	Center of gravity of aircraft
c	Thrust specific fuel consumption
(C_D, C_L)	(Drag, lift) coefficient
C_{D_0}	Parasite drag coefficient
D	Drag force
f_F, f_R	Along-track tire forces for front, rear wheels
Y_F, Y_R	Side tire forces for front, rear wheels
g	Acceleration of gravity
h	Geometric altitude
h_b	Baro-corrected altitude
h_p	Pressure altitude
h_t	Altitude at tropopause
H	Humidity correction
K	Induced drag factor, feedback gains, weighting coefficients
l	Length of wheelbase
l_{ac}	Distance from aerodynamic center to c.g.

l_F	Distance from front wheel to c.g.
l_R	Distance from rear wheel to c.g.
l_{vf}	Distance from vertical fin to c.g.
l_{hs}	Distance from horizontal stabilizer to c.g.
l_a	Standard atmosphere lapse rate
L	Lift force
L_{vt}	Aerodynamic lift from vertical tail
L_{hs}	Aerodynamic lift from horizontal stabilizer
m	Aircraft mass
n	Load factor
M	Mach number
P	Pressure
P_3	Total pressure at combustor inlet -psia
P_{amb}	Ambient pressure -psia(pounds per square inch)
P_{sat}	Saturation vapor pressure -mbar
RH	Relative humidity
s	Path distance
S	Aircraft wing area
T	Engine thrust
T_3	Total pressure at combustor inlet -R
V	Speed at c.g. of aircraft with respect to ground on surface
V_{CAS}	Calibrated airspeed
V_t	True airspeed
W	Aircraft weight
W_h	Speed of vertical wind
W_f	Weight of consumed fuel
$\dot{W}_f$	Fuel flow rate
$\dot{W}_{\mathrm{NO_x}}$	Weight of NOx emissions
$\dot{W}_{\mathrm{CO_2}}$	Weight of CO2 emissions
W_s	Speed of horizontal wind
W_x	East wind component
W_y	North wind component

x	East position
y	North position
α	Steering angle of nose wheel
β	Slide angle of aircraft
η	Lateral deviation of the aircraft c.g. from the centerline
γ	Pitch angle of aircraft
γ_a	Air-relative flight path angle
$\delta = p/p_{SL}$	Pressure ratio
$\theta = \Theta/\Theta_{SL}$	Temperature ratio
Θ	Air temperature
Θ_{amb}	Air temperature -R
Θ_{ambc}	Air temperature -C
κ	Engine throttle setting
ρ	Air density
Φ	Relative humidity
ψ	Orientation of aircraft fuselage measured clockwise from the North
Ψ	Heading of the speed vector measured clockwise from the North
Ψ_a	Air-relative flight heading angle
Ψ_R	Taxiway/runway orientation measured clockwise from the North
ω	Humidity ratio kg water / kg dry air
$()_0$	Initial value
$()_f$	Final value
$()_{min}$	Minimum value
$()_{max}$	Maximum value
$()_c$	Commands related to climb phase
$()_d$	Commands related to descent phase
$()_{cr}$	Commands related to cruise phase
$()_{\mathrm{SL}}$	Sea-level value
$()_{\mathrm{T}}$	Value at tropopause

A.2 Acronyms

AOC	Airline Operations Center, Airline Operational Control
ATC	Air Traffic Control
ATM	Air Traffic Mangament
CAS	Calibrated Speed
EI	Emission Index
ERA	Environmentally Responsible Aviation
FAA	Federal Aviation Administration
FMS	Flight Management System
FL	Flight Level
ICAO	International Civil Aviation Organization
LTO	Landing and Take-Off
NASA	National Aeronautic and Space Adminstration
RTA	Require Time-of-Arrival
TOA	Time of Arrival
TOD	Top of Descent
TS	Trajectory Synthesizer
OFP	Operational Flight Path

Appendix B

Point-Mass Equations of Motion for Aircraft Flight

B.1 Coordinate Systems

Descriptions:

($\hat{I}_s$, $\hat{J}_s$, $\hat{K}_s$): inertial (tatic), earth-centered equatorial

($\hat{I}$, $\hat{J}$, $\hat{K}$): earth-fixed, earth-centered equatorial

($\hat{e}$, $\hat{n}$, $\hat{u}$): topocentric, East, North, up

($\hat{i}$, $\hat{j}$, $\hat{k}$): c.g., wind-axis, $\hat{i}$ along airspeed, $\hat{j} \perp \hat{k}$ and points up, $\hat{j}$ forms right hand system

Assumption: spherical earth, and rotating

$$\begin{bmatrix} \hat{e} \\ \hat{n} \\ \hat{u} \end{bmatrix} = \begin{bmatrix} 0 & 1 & 0 \\ 0 & 0 & 1 \\ 1 & 0 & 0 \end{bmatrix} \begin{bmatrix} \hat{u} \\ \hat{e} \\ \hat{n} \end{bmatrix} \tag{B.1}$$

The following relations can be developed,

$$\vec{\omega}_e = \omega_e \hat{K} \qquad rotationalrateof(\hat{I}, \hat{J}, \hat{K}) \tag{B.2}$$

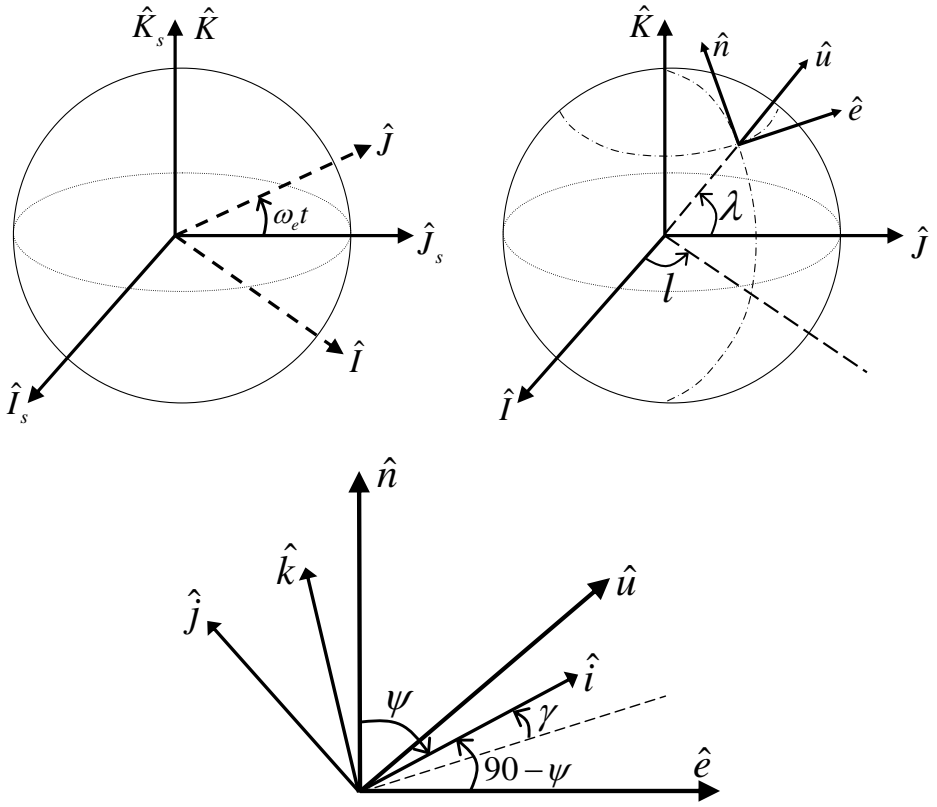

Figure B.1: Relations of frames of references

Then the transformation between $(\hat{I}, \hat{J}, \hat{K})$ and $(\hat{e}, \hat{n}, \hat{u})$ can be developed

$$\begin{aligned}\begin{bmatrix} \hat{u} \\ \hat{e} \\ \hat{n} \end{bmatrix} &= \begin{bmatrix} \cos\lambda & 0 & \sin\lambda \\ 0 & 1 & 0 \\ -\sin\lambda & 0 & \cos\lambda \end{bmatrix} \begin{bmatrix} \cos l & \sin l & 0 \\ -\sin l & \cos l & 0 \\ 0 & 0 & 1 \end{bmatrix} \begin{bmatrix} \hat{I} \\ \hat{J} \\ \hat{K} \end{bmatrix} \\ &= \begin{bmatrix} \cos l\cos\lambda & \sin l\cos\lambda & \sin\lambda \\ -\sin l & \cos l & 0 \\ -\cos l\sin\lambda & -\sin l\sin\lambda & \cos\lambda \end{bmatrix} \begin{bmatrix} \hat{I} \\ \hat{J} \\ \hat{K} \end{bmatrix}\end{aligned} \tag{B.3}$$

or

$$\begin{aligned}\begin{bmatrix}\hat{I}\\ \hat{J}\\ \hat{K}\end{bmatrix} &= \begin{bmatrix}\cos l\cos\lambda & -\sin l & -\cos l\sin\lambda\\ \sin l\cos\lambda & \cos l & -\sin l\sin\lambda\\ \sin\lambda & 0 & \cos\lambda\end{bmatrix}\begin{bmatrix}\hat{u}\\ \hat{e}\\ \hat{n}\end{bmatrix}\\ &= \begin{bmatrix}-\sin l & -\cos l\sin\lambda & \cos l\cos\lambda\\ \cos l & -\sin l\sin\lambda & \sin l\cos\lambda\\ 0 & \cos\lambda & \sin\lambda\end{bmatrix}\begin{bmatrix}\hat{e}\\ \hat{n}\\ \hat{u}\end{bmatrix}\end{aligned} \tag{B.4}$$

$\Rightarrow$

$$\hat{K} = \cos\lambda\hat{n} + \sin\lambda\hat{u} \tag{B.5}$$

In addition

$$\begin{aligned}\begin{bmatrix}\hat{i}\\ \hat{j}\\ \hat{k}\end{bmatrix} &= \begin{bmatrix}\cos\gamma & 0 & \sin\gamma\\ 0 & 1 & 0\\ -\sin\gamma & 0 & \cos\gamma\end{bmatrix}\begin{bmatrix}\cos(90-\Psi) & \sin(90-\Psi) & 0\\ -\sin(90-\Psi) & \cos(90-\Psi) & 0\\ 0 & 0 & 1\end{bmatrix}\begin{bmatrix}\hat{e}\\ \hat{n}\\ \hat{u}\end{bmatrix}\\ &= \begin{bmatrix}\cos\gamma & 0 & \sin\gamma\\ 0 & 1 & 0\\ -\sin\gamma & 0 & \cos\gamma\end{bmatrix}\begin{bmatrix}\sin\Psi & \cos\Psi & 0\\ -\cos\Psi & \sin\Psi & 0\\ 0 & 0 & 1\end{bmatrix}\begin{bmatrix}\hat{e}\\ \hat{n}\\ \hat{u}\end{bmatrix}\\ &= \begin{bmatrix}\cos\gamma\sin\Psi & \cos\gamma\cos\Psi & \sin\gamma\\ -\cos\Psi & \sin\Psi & 0\\ -\sin\gamma\sin\Psi & -\sin\gamma\cos\Psi & \cos\gamma\end{bmatrix}\begin{bmatrix}\hat{e}\\ \hat{n}\\ \hat{u}\end{bmatrix}\end{aligned} \tag{B.6}$$

or

$$\begin{bmatrix}\hat{e}\\ \hat{n}\\ \hat{u}\end{bmatrix} = \begin{bmatrix}\cos\gamma\sin\Psi & -\cos\Psi & -\sin\gamma\sin\Psi\\ \cos\gamma\cos\Psi & \sin\Psi & -\sin\gamma\cos\Psi\\ \sin\gamma & 0 & \cos\gamma\end{bmatrix}\begin{bmatrix}\hat{i}\\ \hat{j}\\ \hat{k}\end{bmatrix} \tag{B.7}$$

$\Rightarrow$

$$\boxed{\begin{aligned}
\hat{i} &= \cos\gamma\sin\Psi\hat{e} + \cos\gamma\cos\Psi\hat{n} + \sin\gamma\hat{u} \\
\hat{e} &= \cos\gamma\sin\Psi\hat{i} - \cos\Psi\hat{j} - \sin\gamma\sin\Psi\hat{k} \\
\hat{u} &= \sin\gamma\hat{i} + \cos\gamma\hat{k} \\
\hat{j} &= -\cos\Psi\hat{e} + \sin\Psi\hat{n}
\end{aligned}} \tag{B.8}$$

B.2 Kinematics

B.2.1 Kinematics of Velocity

The position vector is given by, on a spherical earth,

$$\vec{r} = (R+h)\hat{u} = r\hat{u} \tag{B.9}$$

The rotational velocity of $(\hat{e}, \hat{n}, \hat{u})$ w.r.t. $(\hat{I}, \hat{J}, \hat{K})$ is

$$\vec{\Omega_{enu}} = \dot{l}\hat{K} - \dot{\lambda}\hat{e} \tag{B.10}$$

$$= -\dot{\lambda}\hat{e} + \dot{l}\cos\lambda\hat{n} + \dot{l}\sin\lambda\hat{u} \tag{B.11}$$

We want to find the vehicle velocity w.r.t. Earth

$$\vec{V_e} = (\frac{d\vec{r}}{dt})_{IJK} = \dot{h}\hat{u} + \vec{\Omega}_{enu} \times \vec{r} \tag{B.12}$$

$$= \dot{h}\hat{u} + (-\dot{\lambda}\hat{e} + \dot{l}\cos\lambda\hat{n} + \dot{l}\sin\lambda\hat{u}) \times (R+h)\hat{u} \tag{B.13}$$

$$= \dot{l}(R+h)\cos\lambda\hat{e} + \dot{\lambda}(R+h)\hat{n} + \dot{h}\hat{u} \tag{B.14}$$

On the other hand, the earth-relative velocity can be also expressed as

$$\vec{V_e} = \text{airspeed} + \text{windspeedw.r.t.earth} \tag{B.15}$$

$$= V\hat{i} + (W_e\hat{e} + W_n\hat{n} + W_u\hat{u}) \tag{B.16}$$

$$= V(\cos\gamma\sin\Psi\hat{e} + \cos\gamma\cos\Psi\hat{n} + \sin\gamma\hat{u}) + (W_e\hat{e} + W_n\hat{n} + W_u\hat{u}) \tag{B.17}$$

$$= (V\cos\gamma\sin\Psi + W_e)\hat{e} + (V\cos\gamma\cos\Psi + W_n)\hat{n} + (V\sin\gamma + W_u)\hat{u} \tag{B.18}$$

By comparing the two equations, we have

$$\dot{l}(R+h)\cos\lambda = V\cos\gamma\sin\Psi + W_e \tag{B.19}$$

$$\dot{\lambda}(R+h) = V\cos\gamma\cos\Psi + W_n \tag{B.20}$$

$$\dot{h} = V\sin\gamma + W_u \tag{B.21}$$

or

$$\dot{l} = \frac{V\cos\gamma\sin\Psi + W_e}{(R+h)\cos\lambda} \tag{B.22}$$

$$\dot{\lambda} = \frac{V\cos\gamma\cos\Psi + W_n}{(R+h)} \tag{B.23}$$

$$\dot{h} = V\sin\gamma + W_u \tag{B.24}$$

Additionally, the horizontal ground distance can be obtained as

$$\dot{s} = V\cos\gamma + W_e\sin\Psi + W_n\cos\Psi - \omega_e R\cos\gamma\sin\Psi \tag{B.25}$$

B.2.2 Different Expressions of Wind Components

The wind speed can be expressed in following ways

$$\vec{W} = W_i\hat{i} + W_j\hat{j} + W_k\hat{k} \tag{B.26}$$

$$= W_e\hat{e} + W_n\hat{n} + W_u\hat{u} \tag{B.27}$$

Using Eq. (7)

$$\begin{bmatrix} W_i & W_j & W_k \end{bmatrix}\begin{bmatrix} \hat{i} \\ \hat{j} \\ \hat{k} \end{bmatrix} = \begin{bmatrix} W_e & W_n & W_u \end{bmatrix}\begin{bmatrix} \hat{e} \\ \hat{n} \\ \hat{u} \end{bmatrix}$$

$$= \begin{bmatrix} W_e & W_n & W_u \end{bmatrix}\begin{bmatrix} \cos\gamma\sin\Psi & -\cos\Psi & -\sin\gamma\sin\Psi \\ \cos\gamma\cos\Psi & \sin\Psi & -\sin\gamma\cos\Psi \\ \sin\gamma & 0 & \cos\gamma \end{bmatrix}\begin{bmatrix} \hat{i} \\ \hat{j} \\ \hat{k} \end{bmatrix} \tag{B.28}$$

$\Rightarrow$

$$W_i = \cos\gamma \sin\Psi W_e + \cos\gamma \cos\Psi W_n + \sin\gamma W_u \tag{B.29}$$

$$W_j = -\cos\Psi W_e + \sin\Psi W_n \tag{B.30}$$

$$W_k = -\sin\gamma \sin\Psi W_e - \sin\gamma \cos\Psi W_n + \cos\gamma W_u \tag{B.31}$$

B.3 Velocity Expressions

B.3.1 Earth-Relative Velocity

The earth-relative velocity can be expressed as

$$\vec{V}_e = \vec{V} + \vec{W} \tag{B.32}$$

In terms of $(\hat{e}, \hat{n}, \hat{u})$ system, the Eq. (21)

$$\vec{V}_e = (V\cos\gamma\sin\Psi + W_e)\hat{e} + (V\cos\gamma\cos\Psi + W_n)\hat{n} + (V\sin\gamma + W_u)\hat{u} \tag{B.33}$$

In terms of $(\hat{i}, \hat{j}, \hat{k})$ system

$$\vec{V} = V\hat{i} \tag{B.34}$$

so

$$\vec{V}_e = (V + W_i)\hat{i} + W_j\hat{j} + W_k\hat{k} \tag{B.35}$$

$$= (V + W_e\cos\gamma\sin\Psi + W_n\cos\gamma\cos\Psi + W_u\sin\gamma)\hat{i} \tag{B.36}$$

$$+ (-W_e\cos\Psi + W_n\sin\Psi)\hat{j} \tag{B.37}$$

$$+ (-W_e\sin\gamma\sin\Psi - W_n\sin\gamma\cos\Psi + W_u\cos\gamma)\hat{k} \tag{B.38}$$

B.3.2 Inertial Velocity

Inertial velocity can be expressed as

$$\vec{V}_I = \vec{V}_e + \vec{V}_{e/I} \tag{B.39}$$

where

$$\vec{V}_{e/I} = (\omega_e \hat{K}) \times (R+h)\hat{u} \tag{B.40}$$
$$= \omega_e (R+h)[\cos\lambda \hat{n} + \sin\lambda \hat{u}] \times \hat{u} \tag{B.41}$$
$$= \omega_e (R+h)\cos\lambda \hat{e} \tag{B.42}$$

or

$$\vec{V}_{e/I} = \omega_e (R+h)\cos\lambda[\cos\gamma \sin\Psi \hat{i} - \cos\Psi \hat{j} - \sin\gamma \sin\Psi \hat{k}] \tag{B.43}$$

Define

$$W_e^R = W_e + \omega_e (R+h)\cos\lambda \tag{B.44}$$

Then, in terms of $(\hat{e}, \hat{n}, \hat{u})$ system

$$\vec{V}_I = (V\cos\gamma\sin\Psi + W_e^R)\hat{e} + (V\cos\gamma\cos\Psi + W_n)\hat{n} + (V\sin\gamma + W_u)\hat{u} \tag{B.45}$$
$$= V_{Ie}\hat{e} + V_{In}\hat{n} + V_{Iu}\hat{u} \tag{B.46}$$

Then, in terms of $(\hat{i}, \hat{j}, \hat{k})$ system

$$\vec{V}_I = (V + W_e^R\cos\gamma\sin\Psi + W_n\cos\gamma\cos\Psi + W_u\sin\gamma)\hat{i} \tag{B.47}$$
$$+ (-W_e^R\cos\Psi + W_n\sin\Psi)\hat{j} \tag{B.48}$$
$$+ (-W_e^R\sin\gamma\sin\Psi - W_n\sin\gamma\cos\Psi + W_u\cos\gamma) \tag{B.49}$$
$$= V_{Ii}\hat{i} + V_{Ij}\hat{j} + V_{Ik}\hat{k} \tag{B.50}$$

B.4 External Forces

From the figure,

$$\hat{k}' = -\sin\mu\hat{j} + \cos\mu\hat{k} \tag{B.51}$$

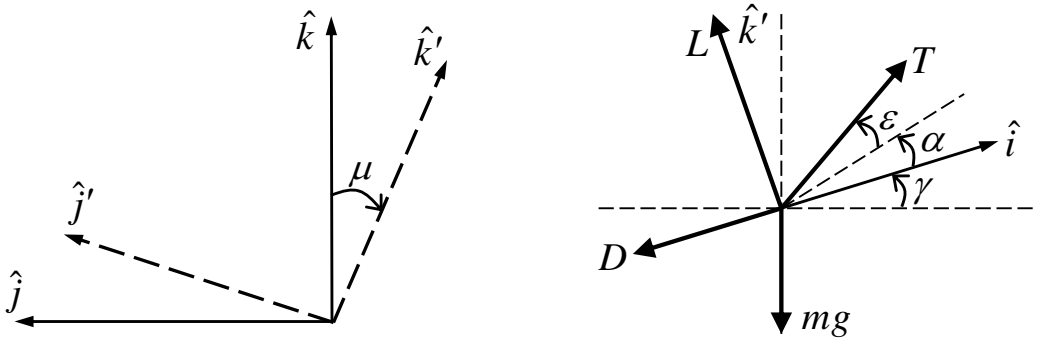

Figure B.2: External forces of aircraft

Assuming zero slide force: $Y = 0$, then

$$\vec{F} = \vec{T} + \vec{D} + \vec{L} + m\vec{g} + \vec{Y} \tag{B.52}$$

where

$$\vec{T} = T\cos(\alpha+\epsilon)\hat{i} + T\sin(\alpha+\epsilon)\hat{k}' \tag{B.53}$$

$$= T\cos(\alpha+\epsilon)\hat{i} - T\sin(\alpha+\epsilon)\sin\mu\hat{j} + T\sin(\alpha+\epsilon)\cos\mu\hat{k} \tag{B.54}$$

$$\vec{L} = L\hat{k}' \tag{B.55}$$

$$= -L\sin\mu\hat{j} + L\cos\mu\hat{k} \tag{B.56}$$

$$\vec{D} = -D\hat{i} \tag{B.57}$$

$$m\vec{g} = -mg\hat{u} = -mg(\sin\gamma\hat{i} + \cos\gamma\hat{k}) \tag{B.58}$$

In terms of $(\hat{i}, \hat{j}, \hat{k})$ system

$$\vec{F} = F_i\hat{i} + F_j\hat{j} + F_k\hat{k} \tag{B.59}$$

$$= [T\cos(\alpha+\epsilon) - D - mg\sin\gamma]\hat{i} \tag{B.60}$$

$$- [L + T\sin(\alpha+\epsilon)]\sin\mu\hat{j} \tag{B.61}$$

$$+ \{[L + T\sin(\alpha+\epsilon)]\cos\mu - mg\cos\gamma\}\hat{k} \tag{B.62}$$

In terms of $(\hat{e}, \hat{n}, \hat{u})$ system

$$\vec{F} = F_e\hat{e} + F_n\hat{n} + F_u\hat{u} \tag{B.63}$$

We have

$$\begin{bmatrix} F_e & F_n & F_u \end{bmatrix} = \begin{bmatrix} F_i & F_j & F_K \end{bmatrix} \begin{bmatrix} \cos\gamma\sin\Psi & \cos\gamma\cos\Psi & \sin\gamma \\ -\cos\Psi & \sin\Psi & 0 \\ -\sin\gamma\sin\Psi & -\sin\gamma\cos\Psi & \cos\gamma \end{bmatrix} \tag{B.64}$$

or

$$F_e = F_i\cos\gamma\sin\Psi - F_j\cos\Psi - F_k\sin\gamma\sin\Psi \tag{B.65}$$

$$F_n = F_i\cos\gamma\cos\Psi + F_j\sin\Psi - F_k\sin\gamma\cos\Psi \tag{B.66}$$

$$F_u = F_i\sin\gamma + F_k\cos\gamma \tag{B.67}$$

B.5 Kinetics

We are interested in the time rates of airspeed component, but the Newton's Law is given in inertial frame

B.5.1 Angular Rates

Angular velocity of $(\hat{I}, \hat{J}, \hat{K})$ w.r.t $(\hat{I}_s, \hat{J}_s, \hat{K}_s)$ is

$$\vec{\omega}_e = \omega_e\hat{K} \tag{B.68}$$

$$= \omega_e(\cos\gamma\hat{n} + \sin\gamma\hat{u}) \tag{B.69}$$

Angular velocity of $(\hat{e}, \hat{n}, \hat{u})$ w.r.t $(\hat{I}, \hat{J}, \hat{K})$ is

$$\vec{\Omega}_{enu} = \dot{l}\hat{K} - \dot{\lambda}\hat{e} \tag{B.70}$$

$$= -\dot{\lambda}\hat{e} + \dot{l}\cos\lambda\hat{n} + \dot{l}\sin\lambda\hat{u} \tag{B.71}$$

Angular velocity of $(\hat{i}, \hat{j}, \hat{k})$ w.r.t $(\hat{e}, \hat{n}, \hat{u})$ is

$$\vec{\omega}_{ijk} = \dot{\Psi}\hat{u} - \dot{\gamma}\hat{j} \tag{B.72}$$

$$= -\dot{\Psi}\sin\gamma\hat{i} - \dot{\gamma}\hat{j} - \dot{\Psi}\cos\gamma\hat{k} \tag{B.73}$$

$$= \dot{\gamma}\cos\Psi\hat{e} - \dot{\gamma}\sin\Psi\hat{n} - \dot{\Psi}\hat{u} \tag{B.74}$$

Angular velocity of of $(\hat{i},\hat{j},\hat{k})$ w.r.t $(\hat{I},\hat{J},\hat{K})$ is

$$\vec{\Omega}_{ijk} = \vec{\Omega}_{enu} + \vec{\omega_{ijk}} \tag{B.75}$$

$$= (-\dot{\lambda} + \dot{\gamma}\cos\Psi)\hat{e} + (\dot{l}\cos\lambda - \dot{\gamma}\sin\Psi)\hat{n} + (\dot{l}\sin\gamma - \dot{\Psi})\hat{u} \tag{B.76}$$

And

$$\vec{V}_{e/I} = \omega_e(R+h)\cos\lambda\hat{e} \tag{B.77}$$

$$\vec{\omega}_e + \vec{\Omega}_{enu} = -\dot{\lambda}\hat{e} + (\omega_e + \dot{l})\cos\lambda\hat{n} + (\omega_e + \dot{l})\sin\lambda\hat{u} \tag{B.78}$$

B.5.2 Velocity Relations

$$\vec{V}_e = \vec{V} + \vec{W} \tag{B.79}$$

$$\vec{V}_I = \vec{V}_e + \vec{V}_{e/I} = \vec{V} + \vec{W} + \vec{V}_{e/I} = \vec{V} + \vec{W}^R \tag{B.80}$$

where

$$\vec{V} = V\hat{i} = V\cos\gamma\sin\Psi\hat{e} + V\cos\gamma\cos\Psi\hat{n} + v\sin\gamma\hat{u} \tag{B.81}$$

$$\vec{W}^R = W_e^R\hat{e} + W_n^R\hat{n} + W_u^R\hat{u} \tag{B.82}$$

$$W_e^R = W_e + \omega_e(R+h)\cos\lambda \tag{B.83}$$

In terms of $(\hat{i},\hat{j},\hat{k})$

$$\vec{W}^R = (W_e^R\cos\gamma\sin\Psi + W_n\cos\gamma\cos\Psi + W_u\sin\gamma)\hat{i} \tag{B.84}$$

$$+ (-W_e^R\cos\Psi + W_n\sin\Psi)\hat{j} \tag{B.85}$$

$$+ (-W_e^R\sin\gamma\sin\Psi - W_n\sin\gamma\cos\Psi + W_u\cos\gamma) \tag{B.86}$$

$$= W_i^R\hat{i} + W_j^R\hat{j} + W_k^R\hat{k} \tag{B.87}$$

B.5.3 Newton's Law for Constant Mass

$$(\frac{d\vec{V}_I}{dt})_{I_sJ_sK_s} = \frac{\vec{F}}{m} \tag{B.88}$$

where

$$(\frac{d\vec{V}_I}{dt})_{I_sJ_sK_s} = (\frac{d\vec{V}_I}{dt})_{IJK} + \vec{\omega}_e \times \vec{V}_I \tag{B.89}$$

$$(\frac{d\vec{V}_I}{dt})_{IJK} = (\frac{d\vec{V}_I}{dt})_{enu} + \vec{\Omega}_{enu} \times \vec{V}_I \tag{B.90}$$

$\Rightarrow$

$$(\frac{d\vec{V}_I}{dt})_{enu} + (\vec{\omega}_e + \vec{\Omega}_{enu}) \times \vec{V}_I = \frac{\vec{F}}{m} \tag{B.91}$$

or

$$(\frac{d\vec{V}_I}{dt})_{enu} + (\frac{d\vec{W}}{dt})_{enu} + (\frac{d\vec{V}_{e/I}}{dt})_{enu} = \frac{\vec{F}}{m} - (\vec{\omega}_e + \vec{\Omega}_{enu}) \times \vec{V}_I \tag{B.92}$$

$\Rightarrow$

$$\boxed{(\frac{d\vec{V}_I}{dt})_{enu} = \frac{\vec{F}}{m} - (\frac{d\vec{W}}{dt})_{enu} - \vec{A}} \tag{B.93}$$

where

$$\boxed{\vec{A} = (\frac{d\vec{V}_{e/I}}{dt})_{enu} + (\vec{\omega}_e + \vec{\Omega}_{enu}) \times \vec{V}_I} \tag{B.94}$$

B.5.4 Expressing in $(\hat{i}, \hat{j}, \hat{k})$

$$(\frac{d\vec{V}_I}{dt})_{enu} = (\frac{d\vec{V}_I}{dt})_{ijk} + \vec{\omega}_{ijk} \times \vec{V} \tag{B.95}$$

$$= \dot{V}\hat{i} + [-\dot{\Psi}\sin\gamma\hat{i} - \dot{\gamma}\hat{j} - \dot{\Psi}\cos\gamma\hat{k}] \times V\hat{i} \tag{B.96}$$

$$= \dot{V}\hat{i} + V\dot{\gamma}\hat{k} - V\cos\gamma\dot{\Psi}\hat{j} \tag{B.97}$$

$$\vec{F} = F_i\hat{i} + F_j\hat{j} + F_k\hat{k} \tag{B.98}$$

$$\begin{aligned}
(\frac{d\vec{W}}{dt})_{enu} =& \dot{W}_e\hat{e} + \dot{W}_n\hat{n} + \dot{W}_u\hat{u} && \text{(B.99)}\\
=& [\dot{W}_e\dot{W}_n\dot{W}_u] \begin{bmatrix} \cos\gamma\sin\Psi & -\cos\Psi & -\sin\gamma\sin\Psi \\ \cos\gamma\cos\Psi & \sin\Psi & -\sin\gamma\cos\Psi \\ \sin\gamma & 0 & \cos\gamma \end{bmatrix} \begin{bmatrix} \hat{i} \\ \hat{j} \\ \hat{k} \end{bmatrix} && \text{(B.100)}\\
=& (\dot{W}_e\cos\gamma\sin\Psi + \dot{W}_n\cos\gamma\cos\Psi + \dot{W}_u\sin\gamma)\hat{i} && \text{(B.101)}\\
&+ (-\dot{W}_e\cos\Psi + \dot{W}_n\sin\Psi)\hat{j} && \text{(B.102)}\\
&+ (-\dot{W}_e\sin\gamma\sin\Psi - \dot{W}_n\sin\gamma\cos\Psi + \dot{W}_u\cos\gamma)\hat{k} && \text{(B.103)}
\end{aligned}$$

$$\boxed{\begin{aligned}\vec{A} &= (\frac{d\vec{V}_{e/I}}{dt})_{enu} + (\vec{\omega}_e + \vec{\Omega}_{enu}) \times \vec{V}_I \\ &= a_i\hat{i} + a_j\hat{j} + a_k\hat{k}\end{aligned}} \tag{B.104}$$

a_i, a_j, a_k are due to Earth rotation & Coriolis Force & spherical earth.

Then we have

$$\boxed{\begin{aligned}
\dot{V} &= \frac{T\cos(\alpha+\epsilon) - D}{m} - g\sin\gamma - \dot{W}_e\cos\gamma\sin\Psi - \dot{W}_n\cos\gamma\cos\Psi - \dot{W}_u\sin\gamma - a_i \\
V\cos\gamma\dot{\Psi} &= \frac{L + T\sin(\alpha+\epsilon)}{m}\sin\mu - \dot{W}_e\cos\Psi + \dot{W}_n\sin\Psi + a_j \\
V\dot{\gamma} &= \frac{L + T\sin(\alpha+\epsilon)}{m}\cos\mu - g\cos\gamma + \dot{W}_e\sin\gamma\sin\Psi + \dot{W}_n\sin\gamma\cos\Psi - \dot{W}_u\cos\gamma - a_k
\end{aligned}} \tag{B.105}$$

B.5.5 Derivations of the A term

$$\begin{aligned}
\vec{A} &= (\frac{d\vec{V}_{e/I}}{dt})_{enu} + (\vec{\omega}_e + \vec{\Omega}_{enu}) \times \vec{V}_I && \text{(B.106)}\\
&= (\frac{d\vec{V}_{e/I}}{dt})_{enu} + \vec{\omega}_e \times (\vec{V} + \vec{W} + \vec{V}_{e/I}) + \vec{\Omega} \times \vec{V}_{e/I} + \vec{\Omega}_e \times (\vec{V} + \vec{W}) && \text{(B.107)}
\end{aligned}$$

where, the term $(\frac{d\vec{V}_{e/I}}{dt})_{enu} + \vec{\omega}_e \times (\vec{V} + \vec{W} + \vec{V}_{e/I})$ comes from earth rotation; $\vec{\Omega} \times \vec{V}_{e/I} + \vec{\Omega}_e \times (\vec{V} + \vec{W})$ comes from spherical earth

from Eq. (44)

$$(\frac{d\vec{V}_{e/I}}{dt})_{enu} = \omega_e[\dot{h}\cos\lambda - \dot{\lambda}(R+h)\sin\lambda]\hat{e} \tag{B.108}$$

$$= \omega_e[\dot{h}\cos\lambda - \dot{\lambda}(R+h)\sin\lambda](\cos\gamma\sin\Psi\hat{i} - \cos\Psi\hat{j} - \sin\gamma\sin\Psi\hat{k}) \tag{B.109}$$

$$\vec{\omega}_e + \vec{\Omega}_{enu} = -\dot{\lambda}\hat{e} + (\omega_e + \dot{l})\cos\lambda\hat{n} + (\omega_e + \dot{l})\sin\lambda\hat{u} \tag{B.110}$$

We have

$$(\vec{\omega}_e + \vec{\Omega}_{enu}) \times \vec{V}_I = \begin{bmatrix} \hat{e} & \hat{n} & \hat{u} \\ -\dot{\lambda} & (\omega_e + \dot{l})\cos\lambda & (\omega_e + \dot{l})\sin\lambda \\ V_{Ie} & V_{In} & V_{Iu} \end{bmatrix} \tag{B.111}$$

$$=(\omega_e + \dot{l})(V_{Iu}\cos\lambda - V_{In}\sin\lambda)\hat{e} \tag{B.112}$$

$$+ [(\omega_e + \dot{l})V_{Ie}\sin\lambda + \dot{\lambda}V_{Iu}]\hat{n} \tag{B.113}$$

$$- [\dot{\lambda}V_{In} + (\omega_e + \dot{l})V_{Ie}\cos\lambda]\hat{u} \tag{B.114}$$

$$=b_e\hat{e} + b_n\hat{n} + b_u\hat{u} \tag{B.115}$$

$$=b_i\hat{i} + b_j\hat{j} + b_k\hat{k} \tag{B.116}$$

$\Rightarrow$

$$\boxed{\begin{aligned} a_e &= \omega_e[\dot{h}\cos\lambda - \dot{\lambda}(R+h)\sin\lambda] + b_e \\ a_n &= b_n \\ a_u &= b_u \end{aligned}} \tag{B.117}$$

Also, substitute Eq. (47) into Eq. (117)-(119)

$$(\vec{\omega}_e + \vec{\Omega}_{enu}) \times \vec{V}_I \tag{B.118}$$

$$=(\omega_e + \dot{l})[\cos\lambda(V\sin\gamma + W_u) - \sin\lambda(V\cos\gamma\cos\Psi + W_n)]\hat{e} \tag{B.119}$$

$$+ [(\omega_e + \dot{l})\sin\lambda(V\cos\gamma\sin\Psi + W_e^R) + \dot{\lambda}(V\sin\gamma + W_u)]\hat{n} \tag{B.120}$$

$$- [\dot{\lambda}(V\cos\gamma\cos\Psi + W_n) + (\omega_e + \dot{l})\cos\lambda(V\cos\gamma\sin\Psi + W_e^R)]\hat{u} \tag{B.121}$$

$$=b_e\hat{e} + b_n\hat{n} + b_u\hat{u} \tag{B.122}$$

$$=b_i\hat{i} + b_j\hat{j} + b_k\hat{k} \tag{B.123}$$

$\Rightarrow$

$$\boxed{\begin{aligned} b_e &= (\omega_e + \dot{l})[\cos\lambda(V\sin\gamma + W_u) - \sin\lambda(V\cos\gamma\cos\Psi + W_n)] \\ b_n &= (\omega_e + \dot{l})\sin\lambda(V\cos\gamma\sin\Psi + W_e^R) + \dot{\lambda}(V\sin\gamma + W_u) \\ b_u &= -(\omega_e + \dot{l})\cos\lambda(V\cos\gamma\sin\Psi + W_e^R) - \dot{\lambda}(V\cos\gamma\cos\Psi + W_n) \end{aligned}} \tag{B.124}$$

using transformation

$$\begin{bmatrix} b_i & b_j & b_k \end{bmatrix} = \begin{bmatrix} b_e & b_n & b_u \end{bmatrix} \begin{bmatrix} \cos\gamma\sin\Psi & -\cos\Psi & -\sin\gamma\sin\Psi \\ \cos\gamma\cos\Psi & \sin\Psi & -\sin\gamma\cos\Psi \\ \sin\gamma & 0 & \cos\gamma \end{bmatrix} \tag{B.125}$$

we have

$$b_i = b_e\cos\gamma\sin\Psi + b_n\cos\gamma\cos\Psi + b_u\sin\gamma \tag{B.126}$$

$$b_j = -b_e\cos\Psi + b_n\sin\Psi \tag{B.127}$$

$$b_k = -b_e\sin\gamma\sin\Psi - b_n\sin\gamma\cos\Psi + b_u\cos\gamma \tag{B.128}$$

therefore

$$\boxed{\begin{aligned} a_i &= \omega_e[\dot{h}\cos\lambda - \dot{\lambda}(R+h)\sin\lambda]\cos\lambda\sin\Psi + b_i \\ &= \{\omega_e[\dot{h}\cos\lambda - \dot{\lambda}(R+h)\sin\lambda] + b_e\}\cos\gamma\sin\Psi + b_n\cos\gamma\cos\Psi + b_u\sin\gamma \\ a_j &= -\omega_e[\dot{h}\cos\lambda - \dot{\lambda}(R+h)\sin\lambda]\cos\Psi + b_j \\ &= -\{\omega_e[\dot{h}\cos\lambda - \dot{\lambda}(R+h)\sin\lambda] + b_e\}\cos\Psi + b_n\sin\Psi \\ a_k &= -\{\omega_e[\dot{h}\cos\lambda - \dot{\lambda}(R+h)\sin\lambda] + b_e\}\sin\gamma\sin\Psi - b_n\sin\gamma\cos\Psi + b_u\cos\gamma \end{aligned}} \tag{B.129}$$

B.5.6 Note

$$\omega_e[\dot{h}\cos\lambda - \dot{\lambda}(R+h)\sin\lambda] = \omega_e[(V\sin\gamma + W_u)\cos\lambda - (V\cos\gamma\cos\Psi + W_n)\sin\lambda] \quad \text{(B.130)}$$

Therefore

$$\boxed{\begin{aligned}\hat{b}_e &= \omega_e[\dot{h}\cos\lambda - \dot{\lambda}(R+h)\sin\lambda] + b_e \\ &= (2\omega_e + \dot{l})[(V\sin\gamma + W_u)\cos\lambda - (V\cos\gamma\cos\Psi + W_n)\sin\lambda]\end{aligned}} \quad \text{(B.131)}$$

and

$$a_i = \hat{b}_e\cos\gamma\sin\Psi + b_n\cos\gamma\cos\Psi + b_u\sin\gamma \quad \text{(B.132)}$$

$$a_j = -\hat{b}_e\cos\Psi + b_n\sin\Psi \quad \text{(B.133)}$$

$$a_k = -\hat{b}_e\sin\gamma\sin\Psi - b_n\sin\gamma\cos\Psi + b_u\cos\gamma \quad \text{(B.134)}$$

then combing with the wind acceleration terms,

$$\boxed{\begin{aligned}A_V &= (\dot{W}_e + \hat{b}_e)\cos\gamma\sin\Psi + (\dot{W}_n + b_n)\cos\gamma\cos\Psi + (\dot{W}_u + b_u)\sin\gamma \\ A_\Psi &= -(\dot{W}_e + \hat{b}_e)\cos\Psi + (\dot{W}_n + b_n)\sin\Psi \\ A_\gamma &= -(\dot{W}_e + \hat{b}_e)\sin\gamma\sin\Psi - (\dot{W}_n + b_n)\sin\gamma\cos\Psi + (\dot{W}_u + b_u)\cos\gamma\end{aligned}} \quad \text{(B.135)}$$

Then the kinetic equations become

$$\dot{V} = \frac{T\cos(\alpha+\epsilon) - D}{m} - g\sin\gamma - A_V \quad \text{(B.136)}$$

$$V\cos\gamma\dot{\Psi} = \frac{L + T\sin(\alpha+\epsilon)}{m}\sin\mu + A_\Psi \quad \text{(B.137)}$$

$$V\dot{\gamma} = \frac{L + T\sin(\alpha+\epsilon)}{m}\cos\mu - g\cos\gamma - A_\gamma \quad \text{(B.138)}$$

checks with Vinh's equations under zero winds. Note Ψ is defined from North here

B.5.7 Complete List of Equations

$$\boxed{\begin{aligned}
\dot{V} &= \frac{T\cos(\alpha+\epsilon)-D}{m} - g\sin\gamma - A_V \\
V\cos\gamma\dot{\Psi} &= \frac{L+T\sin(\alpha+\epsilon)}{m}\sin\mu + A_\Psi \\
V\dot{\gamma} &= \frac{L+T\sin(\alpha+\epsilon)}{m}\cos\mu - g\cos\gamma - A_\gamma \\
\dot{l} &= \frac{V\cos\gamma\sin\Psi + W_e}{(R+h)\cos\lambda} \\
\dot{\lambda} &= \frac{V\cos\gamma\cos\Psi + W_n}{R+h} \\
\dot{h} &= V\sin\gamma + W_u \\
\dot{s} &= V\cos\gamma + W_e\sin\Psi + W_n\cos\Psi - \omega_e R\cos\gamma\sin\Psi
\end{aligned}} \tag{B.139}$$

where

$$L = \frac{1}{2}\rho V^2 S C_L \tag{B.140}$$

$$D = \frac{1}{2}\rho V^2 S C_D \tag{B.141}$$

$$C_D = C_{D_0} + K C_L^2 \tag{B.142}$$

and

$$\boxed{\begin{aligned}
W_e^R &= W_e + \omega_e(R+h)\cos\lambda \\
B_e &= \dot{W}_e + (2\omega_e + \dot{l})[(V\sin\gamma + W_u)\cos\lambda - (V\cos\gamma\cos\Psi + W_n)\sin\lambda] \\
B_n &= \dot{W}_n + (\omega_e + \dot{l})(V\cos\gamma\sin\Psi + W_e^R)\sin\lambda + \dot{\lambda}(V\sin\gamma + W_u) \\
B_u &= \dot{W}_u - (\omega_e + \dot{l})(V\cos\gamma\sin\Psi + W_e^R)\cos\lambda - \dot{\lambda}(V\cos\gamma\cos\Psi + W_n)
\end{aligned}} \tag{B.143}$$

$$\boxed{\begin{aligned}
A_v &= B_e\cos\gamma\sin\Psi + B_n\cos\gamma\cos\Psi + B_u\sin\gamma \\
A_\Psi &= -B_e\cos\Psi + B_n\sin\Psi \\
A_\gamma &= -B_e\sin\gamma\sin\Psi - B_n\sin\gamma\cos\Psi + B_u\cos\gamma
\end{aligned}} \tag{B.144}$$

Assuming wind dependence $W_e(l,\lambda,h), W_n(l,\lambda,h), W_u(l,\lambda,h)$, then

$$A_V(V,\Psi,\gamma,l,\lambda,h;\omega_e,R) \tag{B.145}$$

$$A_\Psi(V,\Psi,\gamma,l,\lambda,h;\omega_e,R) \tag{B.146}$$

$$A_\gamma(V,\Psi,\gamma,l,\lambda,h;\omega_e,R) \tag{B.147}$$

1.
   - if winds also depend on time, $\Rightarrow$ time dependence included
   - if winds only depend on h, or both (λ,h), $\Rightarrow$ l dependence drops
   - in general,
   $$\dot{W}_e = \frac{\partial W_e}{\partial l}\dot{l} + \frac{\partial W_e}{\partial \lambda}\dot{\lambda} + \frac{\partial W_e}{\partial h}\dot{h} \tag{B.148}$$

2. non-rotating earth assumption, $\Rightarrow \omega_e = 0$

3. flat earth, $R \to \infty, \dot{l} \approx 0, \dot{\lambda} \approx 0$, then use

$$\dot{x} = V\cos\gamma\sin\Psi + W_e \tag{B.149}$$

$$\dot{y} = V\cos\gamma\sin\Psi + W_n \tag{B.150}$$

4. rotating earth, $\omega_e \neq 0$, V large or small, W large or small

Appendix C

Equations of Motion for Aircraft Movements on Surface

The aircraft motion for flight can be considered as a point mass, but aircraft motion on surface while taxiing on the airport needs further examination for consideration of rigid body motion when necessary. In this appendix, aircraft equations of motion on a flat surface are systematically derived for use for surface trajectory planning and prediction [2]. It is assumed that the front nose wheel is the steering wheel. The derivation is based on the following assumption:

- Airport surface is horizontally flat
- Nose wheel is the steering wheel
- Tires forces are analyzed in two directions: along-track and cross-track (side)
- Approximations are made assuming low speed motion so that aerodynamic moments are negligible

C.1 Coordinate Systems

Four coordinate systems are used in the derivation of surface equations.

- Inertial frame of reference ($\hat{I}$, $\hat{J}$, $\hat{K}$). The origin is fixed at a certain point on the airport, $\hat{I}$ points to the East, $\hat{J}$ points to the North, and $\hat{K}$ points upward.

- Runway/taxiway system ($\hat{I}_R$, $\hat{J}_R$, $\hat{K}_R$). The origin is at the closest point on the runway/taxiway centerline to the aircraft c.g., $\hat{I}_R$ points to the taxiway centerline, $\hat{K}_R$ points upward, and $\hat{J}_R$ forms a right-handed system with ($\hat{I}_R$, $\hat{K}_R$).
- Aircraft velocity system ($\hat{i}_v$, $\hat{j}_v$, $\hat{k}_v$). The origin fixed at the aircraft center of gravity, $\hat{i}_v$ points to the velocity of the c.g., $\hat{k}_v$ points upward, and $\hat{j}_v$ forms a right-handed system with ($\hat{i}_v$, $\hat{k}_v$).
- Aircraft body system ($\hat{i}_a$, $\hat{j}_a$, $\hat{k}_a$). The origin fixed at the aircraft center of gravity, $\hat{i}_a$ is aligned with the aircraft longitudinal axis, $\hat{j}_a$ is perpendicular to $\hat{i}_a$ and points to the left wing, and $\hat{k}_a$ forms a right-handed system with ($\hat{i}_a$, $\hat{k}_a$).

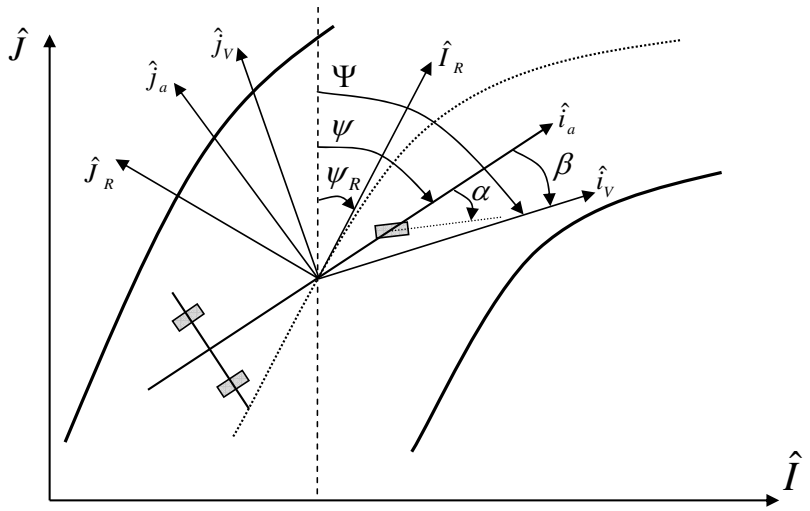

Figure C.1: Coordinates for aircraft movement on surface.

On a flat surface, $\hat{k}_a = \hat{k}_v = \hat{K}_R = \hat{K}$. Fig. C.1 shows that the four coordinates systems and the angles that relate them. Angular relations among these coordinate systems are given below.

C.1.1 Relations with the Inertial System

$$\hat{I}_R = \sin\Psi_R \hat{I} + \cos\Psi_R \hat{J} \tag{C.1}$$

$$\hat{J}_R = -\cos\Psi_R \hat{I} + \sin\Psi_R \hat{J} \tag{C.2}$$

$$\hat{i}_a = \sin\psi\hat{I} + \cos\psi\hat{J} \quad (C.3)$$
$$\hat{j}_a = -\cos\psi\hat{I} + \sin\psi\hat{J} \quad (C.4)$$

$$\hat{i}_v = \sin\Psi\hat{I} + \cos\Psi\hat{J} \quad (C.5)$$
$$\hat{j}_v = -\cos\Psi\hat{I} + \sin\Psi\hat{J} \quad (C.6)$$

and

$$\beta = \Psi - \psi \quad (C.7)$$

C.1.2 Relations with the Runway System

$$\hat{i}_a = \cos(\psi - \Psi_R)\hat{I}_R - \sin(\psi - \Psi_R)\hat{J}_R \quad (C.8)$$
$$\hat{j}_a = \sin(\psi - \Psi_R)\hat{I}_R + \cos(\psi - \Psi_R)\hat{J}_R \quad (C.9)$$

$$\hat{i}_v = \cos(\Psi - \Psi_R)\hat{I}_R - \sin(\Psi - \Psi_R)\hat{J}_R \quad (C.10)$$
$$\hat{j}_v = \sin(\Psi - \Psi_R)\hat{I}_R + \cos(\Psi - \Psi_R)\hat{J}_R \quad (C.11)$$

C.1.3 Relations Between Velocity and Body Axes

$$\hat{i}_v = \cos\beta\hat{i}_a - \sin\beta\hat{j}_a \quad (C.12)$$
$$\hat{j}_v = \sin\beta\hat{i}_a + \cos\beta\hat{j}_a \quad (C.13)$$

$$\hat{i}_a = \cos\beta\hat{i}_v + \sin\beta\hat{j}_v \quad (C.14)$$
$$\hat{j}_a = -\sin\beta\hat{i}_v + \cos\beta\hat{j}_v \quad (C.15)$$

C.2 Velocity and Kinematic Relations

Velocity of the aircraft c.g. is given by

$$\vec{V} = V\hat{i}_v = \dot{x}\hat{I} + \dot{y}\hat{J} = \dot{s}\hat{I}_R + \dot{\eta}\hat{J}_R \tag{C.16}$$

Using the relations among various coordinate systems, we obtain the following kinematic relations.

$$\dot{x} = V\sin\Psi \tag{C.17}$$

$$\dot{y} = V\cos\Psi \tag{C.18}$$

$$\dot{s} = V\cos(\Psi - \Psi_R) \tag{C.19}$$

$$\dot{\eta} = -V\sin(\Psi - \Psi_R) \tag{C.20}$$

The rotational angular velocity of the velocity frame w.r.t the inertial system is given by

$$\overrightarrow{\omega}_v = -\dot{\Psi}\hat{K} = -\dot{\Psi}\hat{k}_v \tag{C.21}$$

The derivative of $\vec{V}$ is given by the Coriolis rule

$$\dot{\vec{V}} = \dot{V}\hat{i}_v + \vec{\omega}_v \times V\hat{i}_v = \dot{V}\hat{i}_v - \dot{\Psi}V\hat{j}_v \tag{C.22}$$

C.3 Free-Body Diagram

In general, forces acting on an airplane moving on an airport surface consist of the following sources of forces

- Engine thrust
- Lift, drag, and side force acting at the aerodynamic center
- weight
- frictional forces, side forces and normal forces from the wheels

- Aerodynamic force from the horizontal stabilizer (HS) and vertical fin (VF)

The following two free-body diagrams illustrate these forces.

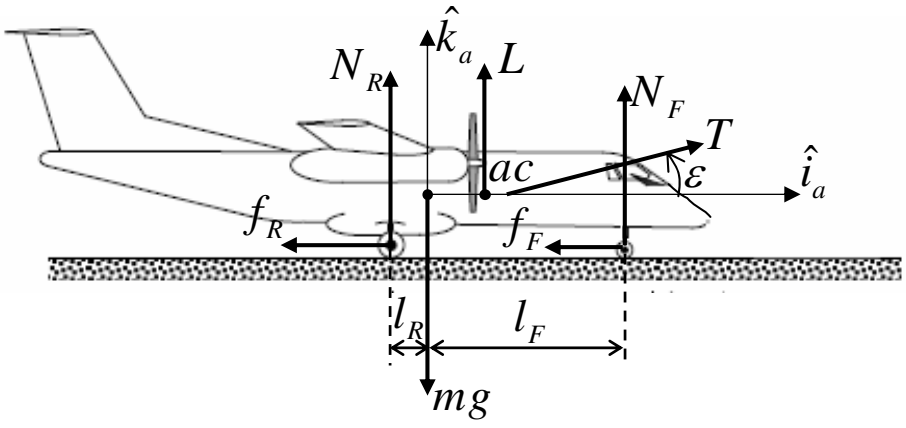

Figure C.2: Free-body diagram: vertical forces and moments.

C.4 Force Expressions

$$\vec{T} = T\cos\epsilon\ \hat{i}_a + T\sin\epsilon\ \hat{k}_a \quad \text{(C.23)}$$

$$\vec{L} = L\ \hat{k}_a \quad \text{(C.24)}$$

$$\vec{D} = -D\cos\beta\ \hat{i}_a + D\sin\beta\ \hat{j}_a \quad \text{(C.25)}$$

$$\vec{Y} = -Y\sin\beta\ \hat{i}_a - Y\cos\beta\ \hat{j}_a \quad \text{(C.26)}$$

$$m\vec{g} = -mg\ \hat{k}_a \quad \text{(C.27)}$$

$$\vec{F}_F = -(f_F\cos\alpha + Y_F\sin\alpha)\ \hat{i}_a + (f_F\sin\alpha - Y_F\cos\alpha)\ \hat{j}_a + N_F\ \hat{k}_a \quad \text{(C.28)}$$

$$\vec{F}_R = -f_R\ \hat{i}_a - Y_R\ \hat{j}_a + N_R\ \hat{k}_a \quad \text{(C.29)}$$

$$\vec{L}_{hs} = L_{hs}\sin i_{hs}\ \hat{i}_a + L_{hs}\cos i_{hs}\ \hat{k}_a \quad \text{(C.30)}$$

$$\vec{L}_{vf} = -L_{vf}\sin i_{vf}\ \hat{i}_a - L_{vf}\cos i_{vf}\ \hat{j}_a \quad \text{(C.31)}$$

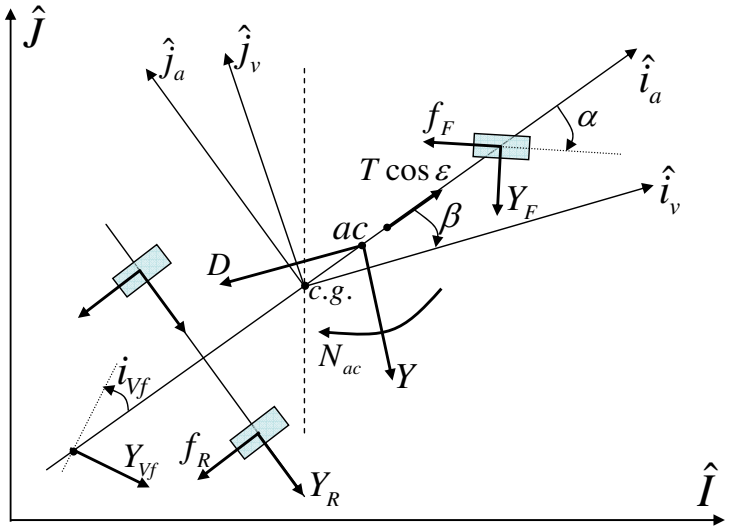

Figure C.3: Free-body diagram: lateral forces and moments.

C.4.1 Components Along Aircraft System

Mathematically,

$$\sum \vec{F} = \vec{T} + (\vec{L} + \vec{D} + \vec{Y}) + m\vec{g} + (\vec{L}_{hs} + \vec{L}_{vf}) + (\vec{f}_w + \vec{Y}_w + \vec{N}_w) \quad \text{(C.32)}$$

$$= F_{ia}\hat{i}_a + F_{ja}\hat{j}_a + F_{ka}\hat{k}_a \quad \text{(C.33)}$$

$$= F_{iv}\hat{i}_v + F_{jv}\hat{j}_v + F_{kv}\hat{k}_v \quad \text{(C.34)}$$

We have

$$F_{ia} = T\cos\epsilon - D\cos\beta - Y\sin\beta - f_F\cos\alpha - Y_F\sin\alpha - f_R + L_{hs}\sin i_{hs} - L_{vf}\sin i_{vf} \quad \text{(C.35)}$$

$$\approx T\cos\epsilon - D\cos\beta - f_F\cos\alpha - Y_F\sin\alpha - f_R \quad \text{(C.36)}$$

$$F_{ja} = D\sin\beta - Y\cos\beta + f_F\sin\alpha - Y_F\cos\alpha - Y_R - L_{vf}\cos i_{vf} \quad \text{(C.37)}$$

$$\approx D\sin\beta + f_F\sin\alpha - Y_F\cos\alpha \quad \text{(C.38)}$$

$$F_{ka} = T\sin\epsilon + L - mg + N_F + N_R + L_{hs}\cos i_{hs} \quad \text{(C.39)}$$

$$\approx T\sin\epsilon + L - mg + N_F + N_R \quad \text{(C.40)}$$

C.4.2 Components Along Velocity System

$$F_{iv} = F_{ia}\cos\beta - F_{ja}\sin\beta \tag{C.41}$$

$$F_{jv} = F_{ia}\sin\beta + F_{ja}\cos\beta \tag{C.42}$$

which results in

$$\begin{aligned} F_{iv} &= T\cos\epsilon\cos\beta - D - f_R\cos\beta + Y_R\sin\beta - f_F\cos(\alpha-\beta) - Y_F\sin(\alpha-\beta) \\ &\quad + L_{hs}\sin i_{hs}\cos\beta + L_{vf}\sin(\beta+i_{vf}) \qquad \text{(C.43)} \\ &\approx T\cos\epsilon\cos\beta - D - f_R\cos\beta + Y_R\sin\beta - f_F\cos(\alpha-\beta) - Y_F\sin(\alpha-\beta) \qquad \text{(C.44)} \end{aligned}$$

and

$$\begin{aligned} F_{jv} &= T\cos\epsilon\sin\beta - Y - f_R\sin\beta - Y_R\cos\beta + f_F\sin(\alpha-\beta) - Y_F\cos(\alpha-\beta) \\ &\quad + L_{hs}\sin i_{hs}\sin\beta - L_{vf}\cos(\beta+i_{vf}) \qquad \text{(C.45)} \\ &\approx T\cos\epsilon\sin\beta - f_R\sin\beta - Y_R\cos\beta + f_F\sin(\alpha-\beta) - Y_F\cos(\alpha-\beta) \qquad \text{(C.46)} \end{aligned}$$

C.5 Moment Expressions

$$\sum \vec{M} = \mathcal{L}\hat{i}_a - \mathcal{M}\hat{j}_a - \mathcal{N}\hat{k}_a \tag{C.47}$$

where

$$\mathcal{L} = 0 \tag{C.48}$$

$$\begin{aligned} \mathcal{M} &= M_{ac} + Ll_{ac} + N_F l_F - N_R l_R - L_{hs}\cos i_{hs} l_{hs} \\ &\approx N_F l_F - N_R l_R \qquad \text{(C.49)} \end{aligned}$$

$$\begin{aligned} \mathcal{N} &= Y l_{ac}\cos\beta + (Y_F\cos\alpha - f_F\sin\alpha)l_F - Y_R l_R - L_{vf}\cos i_{vf} l_{vf} \\ &\approx (Y_F\cos\alpha - f_F\sin\alpha)l_F - Y_R l_R \qquad \text{(C.50)} \end{aligned}$$

C.6 Rigid-Body Equations

C.6.1 Kinetic Equations

According to Newton's second law

$$m\dot{\vec{V}} = m\dot{V}\hat{i}_v - mV\dot{\Psi}\hat{j}_v = F_{iv}\hat{i}_v + F_{jv}\hat{j}_v \tag{C.51}$$

We have

$$m\dot{V} = T\cos\epsilon\cos\beta - D - f_R\cos\beta + Y_R\sin\beta - f_F\cos(\alpha-\beta) - Y_F\sin(\alpha-\beta) \tag{C.52}$$

$$mV\dot{\Psi} = -T\cos\epsilon\sin\beta + f_R\sin\beta + Y_R\cos\beta - f_F\sin(\alpha-\beta) + Y_F\cos(\alpha-\beta) \tag{C.53}$$

C.6.2 Rotational Equations

$$I_k\ddot{\psi} = \mathcal{N} = (Y_F\cos\alpha - f_F\sin\alpha)l_F - Y_R l_R \tag{C.54}$$

or

$$\dot{\psi} = r \tag{C.55}$$

$$\dot{r} = \frac{(Y_F\cos\alpha - f_F\sin\alpha)l_F - Y_R l_R}{I_k} \tag{C.56}$$

C.6.3 Complete List of Rigid-Body Equations

$$\dot{V} = \frac{1}{m}\left[T\cos\epsilon\cos\beta - D - f_R\cos\beta + Y_R\sin\beta - f_F\cos(\alpha-\beta) - Y_F\sin(\alpha-\beta)\right] \tag{C.57}$$

$$\dot{\Psi} = \frac{1}{mV}\left[-T\cos\epsilon\sin\beta + f_R\sin\beta + Y_R\cos\beta - f_F\sin(\alpha-\beta) + Y_F\cos(\alpha-\beta)\right] \tag{C.58}$$

$$\dot{r} = \frac{(Y_F\cos\alpha - f_F\sin\alpha)l_F - Y_R l_R}{I_k} \tag{C.59}$$

$$\dot{\psi} = r \tag{C.60}$$

$$\dot{x} = V\sin\Psi \tag{C.61}$$

$$\dot{y} = V\cos\Psi \tag{C.62}$$

where the last two equations may also be expressed as (x, η), and β is the slide angle, which is the angle between aircraft velocity and aircraft's orientation.

$$\dot{s} = V\cos(\Psi - \Psi_R) \tag{C.63}$$

$$\dot{\eta} = -V\sin(\Psi - \Psi_R) \tag{C.64}$$

and

$$\beta = \Psi - \psi \tag{C.65}$$

C.6.4 Algebraic Relations

From the following relations

$$F_{ka} = 0 \tag{C.66}$$

$$\mathcal{M} = 0 \tag{C.67}$$

one obtains

$$0 = N_F + N_R + T\sin\epsilon + L - mg \tag{C.68}$$

$$0 = N_F l_F - N_R l_R \tag{C.69}$$

or

$$N_F = (mg - L - T\sin\epsilon)\frac{l_R}{l_F + l_R} \tag{C.70}$$

$$N_R = (mg - L - T\sin\epsilon)\frac{l_F}{l_F + l_R} \tag{C.71}$$

C.6.5 Aerodynamic Supporting Relations

Because V was defined as velocity with respect to ground, to compute aerodynamic force, aircraft's velocity with respect to air should be defined (V_a).

$$V_a = V - V_w \tag{C.72}$$

Where V_w is component of wind velocity with respect to the ground in direction of aircraft motion.

$$L = \frac{1}{2}\rho V_a^2 S C_L \tag{C.73}$$

$$D = \frac{1}{2}\rho V_a^2 S C_D \tag{C.74}$$

$$L_{hs} = \frac{1}{2}\rho V_{hs}^2 S_{hs} C_L(i_{hs}) \quad \text{(C.75)}$$

$$L_{vf} = \frac{1}{2}\rho V_{vf}^2 S_{vf} C_L(i_{vf}) \quad \text{(C.76)}$$

C.6.6 Tire Force Relations

The following tire force relations are needed. They depend on N_R, N_F, $\alpha - \beta$, and properties of road conditions tire.

$$f_R = f_R(N_R; \mathcal{T}, \mathcal{R}) \quad \text{(C.77)}$$

$$Y_R = Y_R(N_R; \mathcal{T}, \mathcal{R}) \quad \text{(C.78)}$$

$$f_F = f_F(N_F; \alpha - \beta, \mathcal{T}, \mathcal{R}) \quad \text{(C.79)}$$

$$Y_F = Y_F(N_F; \alpha - \beta, \mathcal{T}, \mathcal{R}) \quad \text{(C.80)}$$

where $\mathcal{T}$ and $\mathcal{R}$ represent general tire and road conditions. Modeling of these relations is discussed in the Appendix.

C.7 2D Point Mass Model

Assuming $\beta \approx 0$ or $\psi \approx \Psi$, we obtain a point-mass model.

$$\dot{V} = \frac{1}{m}\left[T\cos\epsilon - D - f_R - f_F\cos\alpha - Y_F\sin\alpha\right] \quad \text{(C.81)}$$

$$\dot{\Psi} = \frac{1}{mV}\left[Y_R - f_F\sin\alpha + Y_F\cos\alpha\right] \quad \text{(C.82)}$$

$$\dot{x} = V\sin\Psi \quad \text{(C.83)}$$

$$\dot{y} = V\cos\Psi \quad \text{(C.84)}$$

where the last two equations may also be expressed as (x, η).

$$\dot{s} = V\cos(\Psi - \Psi_R) \quad \text{(C.85)}$$

$$\dot{\eta} = -V\sin(\Psi - \Psi_R) \quad \text{(C.86)}$$

C.8 1-D Point Mass Model

Assuming that the aircraft can following the centerline of the taxiway and runway perfectly

$$\Psi = \Psi_R(s) \;\; \eta = 0 \quad \text{(C.87)}$$

resulting

$$\dot{\Psi} = \frac{d\Psi_R}{ds} V \tag{C.88}$$

which uniquely determines α_c from

$$f_F \sin\alpha_c - Y_F \cos\alpha_c = Y_R - mV^2 \frac{d\Psi_R}{ds} \quad \Rightarrow \quad \alpha_c \tag{C.89}$$

Any constraint on speed and the shape of runway translate into constraint on the steering angle.

The 1-D point-mass equations become

$$\dot{V} = \frac{1}{m}\left[T\cos\epsilon - D - f_R - f_F\cos\alpha_c - Y_F \sin\alpha_c\right] \tag{C.90}$$

$$\dot{s} = V \tag{C.91}$$

For near straightline motions, $\alpha_c \approx 0$, the equations become

$$\dot{V} = \frac{1}{m}\left[T\cos\epsilon - D - f_R - f_F\right] \tag{C.92}$$

$$\dot{s} = V \tag{C.93}$$

C.9 1-D Kinematic Model

In a 1-D kinematic model, speed V is assumed to be the control, so there is only only equation left.

$$\dot{s} = V \tag{C.94}$$

However, for applications where noise or fuel burn are needed, one still needs to calculate the corresponding thrust. This may be done from

$$T\cos\epsilon = m\dot{V} + D + f_R + f_F\cos\alpha_c + Y_F\sin\alpha_c \tag{C.95}$$

Variations of the speed profile must be properly selected to make sure they are physically feasible, or the resulting thrust is within its physical bounds.

C.10 Model of Tires Forces

This section gives a brief discussion about tires forces of aircraft on surface. Here, we are primarily concerned with the longitudinal tire force f_F and lateral tire force Y_F. The

longitudinal forces for front and rear tire are represented by f_F and f_R respectively, which can be modeled as,

$$f_F = C_{\sigma F}\sigma_F \tag{C.96}$$

$$f_R = C_{\sigma R}\sigma_R \tag{C.97}$$

Where $C_{\sigma F}$ and $C_{\sigma R}$ are called longitudinal tire stiffness parameters of front and rear tire respectively. σ_F and σ_R are slip ratios for front and rear tires respectively, which are the difference between the actual longitudinal velocity at the axle of the wheel V_{ax} and the equivalent rotational velocity $r_w\omega_w$ of the tire, given by:

$$\sigma = \frac{r_w\omega_w - V_{ax}}{V_{ax}} \tag{C.98}$$

Physically, slip ratios σ_F and σ_R depends on connection situation between tire and road, of which normal force between tire and road is a part. The normal force for front and rear tires was briefly computed in eq

Therefore, the longitudinal forces f_F and f_R depends on tire stiffness parameters, road conditions, connection between road and tire as well. To simplify computational work, a brief model related with normal force can be used

$$f_F = C_f N_F \tag{C.99}$$

$$f_R = C_f N_R \tag{C.100}$$

Where, C_f is denoted as longitudinal friction coefficient. In this paper, depending on aircraft tire stiffness and road condition, C_f is chosen to be 0.02.

The lateral forces for front and rear tire are represented by Y_F and Y_R respectively, can be modeled as.

$$Y_F = C_a a_F \tag{C.101}$$

$$Y_R = C_a a_R \tag{C.102}$$

Where is C_a called cornering stiffness, a_F and a_R are the slip angles for the front and rear tires respectively, is defined as the angle difference between the orientation of the tire and the orientation of the velocity vector of the vehicle at that tire. Because only

front tire has steering angle, then

$$a_F = \alpha - \theta_F \tag{C.103}$$

$$a_R = 0 \tag{C.104}$$

Where, θ_F are velocity angle at front tire, can be computed by aircraft velocity V and motion slip angle β,

$$\theta_F = \frac{V \sin\beta + l_F \dot{\psi}}{V \cos\beta} \tag{C.105}$$

C.11 Approximation: Steady Turning Relations

When aircraft is turning at a constant steering angle α, consider a model of aircraft geometry as shown in Fig. C.4. In the model, the front wheel (turning wheel) is represented by A, two rears wheels are represented by B and C. The steering angle for front wheel is represented by α. Then center of gravity of the aircraft is at point $c.g$. The distances of front wheel and rear wheels from the c.g of the aircraft are l_F and l_R respectively. The wheelbase of the aircraft is $l = l_F + l_R$.

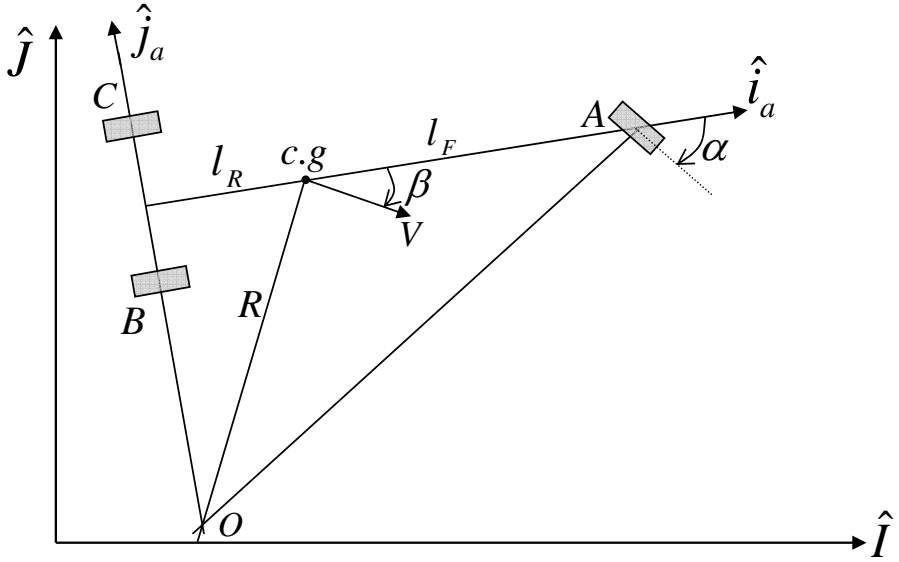

Figure C.4: Geometry of aircraft's wheel base

The direction of nose wheel of aircraft makes an angle α with $\hat{i}_a$ direction. Assume

instantaneous radius of trajectory of aircraft is defined by the length of the line which connects the c.g. to the instantaneous rolling center O. The direction of velocity V is perpendicular to the line , makes an angle β with $\hat{i}_a$ direction. Then base on these geometries, a equation governing the system is derived.

$$\tan\beta = l_R \tan\alpha / l \tag{C.106}$$